A study of wave propagation and stiffness anisotropy in anisotropically loaded granular material-synthetic fiber binary systems

Haiwen Li[1], Jing Ren[2], Kostas Senetakis[3] and Matthew Coop[4]

[1] **H. Li**, Civil Engg., MSc, PhD
Geotechnical Engineer
Geotechnical Design & Installation
EPC & Operations
Ørsted, Copenhagen, Denmark
Email: haili@orsted.com

[2] **J. Ren**, Civil Engg., MSc, PhD student
Department of Architecture and Civil Engineering
City University of Hong Kong, Hong Kong SAR
Email: jinren6-c@my.cityu.edu.hk

[3] **K. Senetakis**, Civil Engg., MSc, PhD
Associate Professor,
Department of Architecture and Civil Engineering
City University of Hong Kong, Hong Kong SAR
Email: ksenetak@cityu.edu.hk
*Corresponding Author

[4] **M. R. Coop**, Civil Engg., PhD
Professor,
Department of Civil, Environmental and Geomatic Engineering
University College of London, London, UK.
Email: m.coop@ucl.ac.uk

Abstract

The influence of polypropylene fiber inclusion on the wave propagation parameters and stiffness anisotropy of granular materials was examined through vertically and laterally positioned bender elements, by which, shear wave velocities were measured leading to the quantification of elastic stiffness $G_{max(vh)}$, $G_{max(hv)}$ and $G_{max(hh)}$ (the first subscript corresponds to the direction of wave propagation and the second subscript corresponds to the direction of particle perturbation as v:vertical and h:horizontal). Various stress paths were considered to comprehensively study stiffness anisotropy of the specimens and grain-scale laboratory tests were additionally performed to provide, partly, some multi-scale insights into the mechanisms of wave propagation of the sand-fiber granular composites. For the back-calculation of elastic stiffness from the wave propagation experiments, Biot's theory was adopted, in which case an equivalent density was used to interpret the high-frequency test results taking into account the relative movement of the solid and fluid phases, which approach provided much better convergency of the results from bender elements and resonant column tests. In this case we assumed that the solid skeleton is composed of the sand particles and the fibers. The test results indicated that when subjected to isotropic stress state, the presence of fibers led to a decrease of $G_{max(vh)}$ and $G_{max(hv)}$ but an increase of $G_{max(hh)}$. The extent of $G_{max(hh)}$ increase was dependent on the characteristics of the host sand and could be attributed to the structural anisotropy with preferred horizontal orientation of the fibers leading to more pronounced development of rigid-soft contacts in the vertical direction. The contribution of the rigid-soft contacts in stiffness reduction could be linked to the microscopic influence of the softer synthetic fibers in reducing the normal contact stiffness and increasing the energy dissipation of the granular system as the grain-scale experiments suggested. When subjected to anisotropic stress state, the stiffness anisotropy was affected by fiber content in a way that with increasing amount of fiber inclusion, the reduction of the stiffness anisotropy became larger. The stiffness anisotropy of the sand or sand-fiber binary system increased with the increase of the stress ratio. Further analysis of the test results revealed that stress induced anisotropy was directly linked to the influence of deviatoric stress on the volumetric strain.

Keywords: Granular material; polypropylene fibers; wave propagation; stiffness; stiffness anisotropy; stress anisotropy; rigid-soft contacts.

1. Introduction

In the literature of ground improvement, there are different types of geosynthetics with potentially promising applications, including planar types, geosynthetics in granular form and also fibrous-type geosynthetics. However, a larger portion of research and practice has focused on planar types of geosynthetics and there are many gaps in our knowledge with respect to the fundamental mechanisms of fibrous inclusions in granular materials. On a practical standpoint, reinforcing soils with fibrous-type inclusions has been found to be a promising solution to improve the engineering performance of geo-systems [1-7]. Experimental studies have indicated noticeable reinforcement effects of fibers when mixed with soils in improving their shear strength and ductility, reducing the liquefaction susceptibility and the post-peak strength loss [8-16].

Despite significant progress being made to understand the static mechanisms of fiber-reinforced soils, studies which examine the influence of fibers on the wave propagation parameters and stiffness of these composite granular systems are limited [17-22]. Wave propagation parameters are very important to be measured and modeled, as their assessment is critical to be obtained in the prediction of deformations of geo-systems subjected to static and dynamic loads [23-24]. They also contribute to the fundamental study and characterization of granular materials/sedimentary profiles and the analysis of energy transport and dissipation mechanisms in granular systems [25-31]. Previous studies have highlighted the significant impact of micro-scale parameters, contact stiffness or the brittle to elastoplastic-to-brittle behavior at the contacts of the grains on their wave propagation/elastic parameters [25, 32-36]. Yimsiri and Soga [37] demonstrated that because of the influence of surface (micro-scale) roughness, granular materials have a stiffness – pressure relationship which deviates from what the Hertz theory would suggest. Additionally, micro-scale parameters have been demonstrated to play key role in linking morphology and elastic properties of particles with their macro-scale nonlinear behavior and energy dissipation mechanisms [36-39]. Binary granular materials including sand-fiber composites, display significant complexity in their behavior with competitive mechanisms to be encountered with respect to energy transport and dissipation as recent theoretical and experimental studies have shown [40-42]. This adds further difficulties in the constitutive modeling of these systems compared, for example, to the analysis of soil-planar block interactions. In these complex systems, the competition between rigid, rigid-soft and soft contacts governs their constitutive behavior and the transmission of waves/energy dissipation.

In binary granular material – fiber systems, the literature would suggest that the inclusion of fibers increases significantly the shear strength of the bulk material which has been attributed to the mobilization of fibers in tension [1-8, 11]. However, published data have suggested that, in general, the inclusion of fibers decreases the shear wave velocity and elastic stiffness. However, this influence will depend upon a combination of granular material type, fiber type and content, the stress path and strain level in consideration as well as the orientation of the fibers. For polypropylene fibers [20, 22], carbon fibers [19] and recycle carpet fibers [43], mixed with different types of sands, data published in the literature have suggested a decrease of stiffness measured at small strains (i.e., elastic stiffness) compared with that of the host soil. These studies have examined the stiffness of soils based on wave propagation analysis along the axis of the specimen (vertical propagation) while particle perturbations take place radially (horizontally). In this case $G_{max(vh)}$ is the major stiffness component reported in previous works. However, in many practical problems such as the understanding of the sedimentation processes and the influence of bedding plane direction, or the fundamental study of the response of granular materials, the knowledge of the stiffness in different directions is important to be obtained [44-47]. This includes $G_{max(hv)}$ (waves propagating in the horizontal direction with the particles vibrating in the vertical direction) and $G_{max(hh)}$ (wave propagation and particle vibration both take place in the horizontal direction). With respect to clayey (i.e., cohesive granular systems) and sandy soils (i.e., cohesionless granular systems), many research works have described the cross-anisotropic behavior of geo-materials [48-53] and also the strong dependency of the type of the granular material on the influence of stress path and stress history on stiffness and stiffness anisotropy [54]. For binary (composite) granular materials, wave transmission in different directions is controlled by the development of rigid, rigid-soft and soft interfaces leading to higher level of anisotropy (both in terms of structural and stiffness anisotropy) [41]. This gives a lot of scope in the study and fundamental understanding of energy transport and dissipation in composite granular systems, which in the present study is approached through the analysis of stiffness from the measured shear wave velocities. This can be particularly useful to provide some inferences between stiffness anisotropy and fabric anisotropy as well, as the orientation of the fibers typically forms an anisotropic structure.

The fabric which develops as a result of the applied method to construct laboratory specimens for testing, in attempts to reproduce natural processes of deposition and diagenesis in natural deposits, has a notable impact on the mechanical response of soils. For soil-fiber binary systems, which are engineered composite granular materials, the preparation process influences the whole soil-fiber structure including the distribution and orientation of the fibers. It has been suggested in the literature that fiber orientations resulting from the moist tamping fabrication technique are likely to be anisotropic with a preferred horizontal bedding plane [2, 55-56]. Fiber orientation largely governs their contribution to the strength of binary fiber-reinforced systems [57-59]. However, the influence of fiber orientation on the wave propagation characteristics (and subsequently on the stiffness of granular materials measured at small strains) has been largely overlooked, which was one of the major motivations behind the present study.

The purpose of this work is to examine the impact of fiber content on the wave propagation parameters and stiffness anisotropy of sand-fiber composite materials subjected to various stress paths (both isotropic and anisotropic), providing in this way a new contribution into the examination of the influence of fibrous synthetic inclusion on the constitutive response of granular materials. Particular focus of this investigation is the examination of the behavior of these binary systems at small strains (i.e., wave propagation and elastic parameters). Additional multi-scale insights were obtained performing grain-scale experiments on sand particle-fiber-sand particle microscopic samples emphasizing on the influence of fiber inclusion in the normal contact response of sand grain contacts. Particularly the analysis of the grain-scale experiments provided, through the quantification of contact stiffness, some additional insights in understanding the stiffness reduction of fiber-sand composite systems when the waves are propagating along the axis of the specimen, while particle motion takes place radially ($G_{max(vh)}$ and $G_{max(hv)}$). We need to notice that the macroscopic experimental data would be influenced by the sample preparation method adopted in the present work, which resulted in predominantly horizontally oriented fibers. This could give scope for future studies to further examine the relationship of stiffness anisotropy – fiber content – structural characteristics of these composites.

2. Materials and testing program

2.1 Materials used for the macroscopic experiments

The macroscopic experiments in the present study, i.e., element-size samples subjected to bender element tests, were performed using two sand-sized fractions of a basaltic crushed rock (a well-graded fraction: BS1, and a uniform fraction: BS2) and also Sydney sand (SS), which is a natural poorly-graded soil. For the microscopic tests (Section 2.5), Sydney sand was replaced with LBS (Leighton Buzzard sand) because of limitations with respect to the particle size to be tested in the grain-scale apparatus. Note that SS and LBS have very similar characteristics in terms of particle morphology and they are both composed of quartz as the major mineral, though Sydney sand consists of grains with slightly rougher surfaces. Both materials (SS, LBS, BS) have a specific gravity of solids of 2.65. The particle shape of the materials was quantified through visual observations from optical and scanning electron microscope (SEM) images in conjunction with an empirical chart which was originally proposed by Krumbein and Sloss [60] and later modified by Cho et al. [61] and the results from this analysis are summarized in Table 1. Sydney sand has an average regularity of 0.65, which implies that it has sub-rounded particles. BS1 and BS2 have irregularly shaped particles with an average regularity of 0.41. Note that the average regularity equals to the mean value of roundness and sphericity (taken as an arithmetic mean value) as assessed on a representative sample of grains from each granular material. Despite the development of more advanced techniques in particle shape characterization (e.g., [62-63]), the application of the empirical approach adopted in the present study provides an effective means in incorporating particle shape influences in the examination of wave propagation and energy dissipation in granular systems [61, 64-65].

Sydney sand and BS2 have the same coefficient of uniformity and so the study of sand-fiber mixtures with these two materials as the host sands helped to provide insights into the impact of particle shape of the host granular material on the behavior of the mixtures. BS1 and BS2 have the same particle shape but different coefficients of uniformity, so that the study of sand-fiber mixtures with these two materials as the host sands helped to examine the impact of particle grading. A summary of the properties of the different sands is given in Table 1 and the grading curves of the three soils are schematically shown in Figure 1. Representative scanning electron microscope images of the two sands are given in supplementary Figure 1. Tian et al. [66] examined the surface roughness (in terms of RMS) values of LBS and Blue sand and reported that Blue sand has grains with much rougher surfaces. RMS roughness values for LBS have been reported within a range of 0.20 to 0.45 μm [66-68], however Blue sand grains have, approximately, five to ten times higher RMS roughness compared with LBS [66]. Flattened three-dimensional surface profiles of the two sands taken from an interferometer are given in supplementary Figure 2 (corresponding to representative samples). The analysis on representative samples from the two sands in the present study confirmed the range of values as reported by [66-68]. For the Sydney sand, the interferometry tests on a representative sample of grains indicated an average RMS roughness of 0.49 μm (Supplementary Table 1 gives a summary of the roughness measurements for Sydney sand specimens). In general, the RMS roughness values of the Sydney sand were found to be on the upper bound of values for LBS.

As synthetic material, polypropylene fibers with a length of 12 mm and a diameter of 0.03mm (circular cross section) were used in the study to determine their influence on the wave propagation and stiffness of the sand-fiber composites. The specific gravity of the polypropylene fibers is 0.9. Their average tensile resistance is equal to 120 MPa, and they have negligible bending resistance. The contents of fiber by mixture weight ranged from 0 to 2%.

2.2 Specimen preparation for the macroscopic experiments

The macroscopic experiments were carried out on specimens constructed in a stress path triaxial apparatus (h=152 mm, d=76 mm, where h and d correspond to the length and diameter, respectively) and also in a fixed-partly fixed resonant column of the Hardin-type (h=140 mm, d=70 mm). Schematic illustrations of these two experimental setups are given in Figures 2 and 3. Each specimen was constructed in several layers of approximately equal thickness using the moist tamping technique for the sand-fiber mixtures, which were subsequently tested in a fully saturated state. This specimen construction method is often used in laboratory studies of sand-fiber binary systems and it has the advantage of good control of specimen density while mitigating segregation of the particles [55-57, 69]. It produces a fabric which resembles that of a compacted reinforced soil in the field [69]. To illustrate the orientation of the fibers based on the sample preparation method used in the present study, one specimen was prepared and compacted in a metal mold (BS1 with 0.5% fibers) using a water content of 3%-5%, approximately. Subsequently, the sample was placed in a freezer for about 12 hours at a temperature of -50 °C. The frozen sample was then cut in vertical and horizontal directions (Figure 4(a)). A Leica M80 stereomicroscope and a Leica IC80 HD camera were used to capture images taken from cross-sections of the specimen. Figures 4(b) and 4(c) show images taken from the horizontal plane, and based on this, it was observed that the fibers were randomly distributed. From the images in Figures 4(d) and 4(e), which were taken from the vertical plane of the specimen and rotated 90 degrees, it is observed that the fibers are oriented, predominantly, horizontally. The study by Soriano et al. [56] utilized the X-ray tomography technique to examine the fabric of sand-fiber mixtures. That study showed that the moist tamping sample preparation method creates anisotropic fiber orientation with preferential sub-horizontal directions. For polypropylene fibers it is technically difficult to analyze images from micro-CT scanning because their specific gravity is equal to 0.9, which is relatively close to that of water and thus, Soriano et al. [56] used fluorocarbon fibers with specific gravity of 1.7 which could make it feasible to detect the fibers in the X-ray tomography. Nonetheless, the basic characterization of fibers' orientation from the images in Figure 4 matches that from the study by Soriano et al. [58] and will be a basis to provide some of the interpretations in the consecutive sections, even though it is acknowledged that the influence of fiber orientation on stiffness/stiffness anisotropy would worth further investigation, for example by changing the sample preparation method in future studies.

Detailed description of the experimental procedure including system set up and saturation process after specimen preparation is provided by [18, 20]. Dry tamping was used for most of the pure sand specimens (detailed in Table 2), as there were no segregation problems. Several pure sand specimens were prepared by moist tamping to confirm that dry tamping and moist tamping preparation methods provide similar results in terms of wave propagation parameters.

2.3 Test procedure: macroscopic experiments

A stress path triaxial apparatus mounted with lateral bender element (BE) inserts was employed to measure the shear wave velocities $V_{s(hv)}$ and $V_{s(hh)}$, while the resonant column (RC) apparatus (equipped with a pair of BE on the top and bottom platens) was used to measure $V_{s(vh)}$. Li et al. [70] presented the calibration details of the RC system. After the saturation process was completed, each specimen was consolidated at a target pressure and subsequently subjected to a chosen stress path (isotropic or anisotropic) with bender element measurements taken along this path. For each specimen, the axial strain was directly recorded with a vertically positioned displacement transducer (LVDT), and sample volume changes were recorded using a volume/pressure controller. For the dry specimens, the volumetric strain was assumed to be equal to three times the axial strain (after [50, 64]). Note that even if the error in the estimated volumetric strain were 100%, which is an extreme case, the resultant error in the measured elastic stiffness (G_{max}) is expected to be no more than 3% to 4% [71]. Additionally, a specially designed mould was used so that the bender element inserts were placed in advance prior to the construction of the specimens. As the bender element inserts were sealed, this provided the necessary mitigation of leakage/contact with air to prepare the cohesionless samples.

2.4 Testing program: macroscopic experiments

Two sets of “macroscopic” tests were conducted and details of each set are provided in Tables 2 and 3. The specimens summarized in Table 2 were subjected to an isotropic stress path to study the exclusive effect of fiber orientation. The mean effective confining pressure (p'), which is an isotropic pressure for this set of tests, ranged from 50 kPa to 1600 kPa. For specimens in Table 3, anisotropic stress was applied to examine the impact of stress induced anisotropy on elastic wave propagation and stiffness. After the completion of the isotropic consolidation, for specimen no. 28 to specimen no. 34 in Table 3, a constant p' loading path was followed, and p' was maintained at 100 kPa and the stress ratio (q/p') where stiffness was measured followed a sequence of 0, 0.25, 0.5, 0.75, 1 and 1.2 (note that q denotes the deviatoric stress and p' denotes the mean effective confining pressure). Specimens no. 35 to no. 38 were consolidated isotopically and then were subjected to extension stress paths under constant p'=100 kPa (q/p' followed a sequence of -0.1, -0.2, -0.3, -0.4 to -0.5). For these specimens, after they reached the desired stress ratio in extension, the stress anisotropy was removed bringing back the stress state to the isotropic condition. These specimens were subsequently loaded under a constant p' compression stress path (q/p' ranging from 0 to 1). Finally, these specimens were unloaded to the isotropic stress state. In summary, specimen no.35 to specimen no.38 were subjected to constant p' extension, loading and unloading, followed by constant p' compression, loading and unloading. Therefore, the values of the stress ratio ranged from -0.5 to 1 (Table 3). The different applied stress paths are illustrated in Figure 5.

2.5 Microscopic experiments

Understanding of the bulk response of granular (and composite) materials, necessitates an investigation of their microscopic behavior such as grain contact parameters as multi-scale studies would suggest [42, 72-74]. For this purpose, in order to enrich the discussions from the wave propagation experiments, an additional set of microscopic (grain-scale) tests was conducted in the present study, in which case, as mentioned earlier in the paper, Sydney sand was replaced with

LBS. Thus, the microscopic tests investigated the contact behavior of LBS – fiber and Blue sand – fiber specimens. The grain-scale experiments were used to provide some additional support of the macroscopic observations, particularly emphasizing the influence of fiber inclusion on the normal contact response of sand grain contacts. For these tests, a grain-scale apparatus was used [38, 75] and a schematic illustration of the apparatus is given in Figure 6. This is a custom-built experimental setup which is composed of two loading arms (one in the horizontal direction and one in the vertical direction) each consisting of high precision load cell and non-contact displacement sensor, as well as a set of mechanical connections and small linear bearing systems. The apparatus is particularly designed to test small in size samples, for example the frictional behavior of sand grain contacts with a size between about 0.5 to 5mm (average diameter of particles). Detailed presentation of the calibration of this apparatus has been described by He et al. [75].

A similar approach as the one described by Li et al. [42] was used to prepare the sand-fiber samples for the grain-scale tests. Sizes of around 1-2mm particles from LBS and Blue sand were used for these experiments and the fibers were placed on the lower grain, prior to bringing the upper grain downwards so that to apply the normal load to the contact. All the microscopic tests (i.e., pure sand grain samples and sand grain-polypropylene fiber samples) were performed applying a maximum normal load of 3N and recording the normal load – displacement response of the samples. In this case, the measured displacements corresponded to “global” deformations at the contact of the sand grain – fiber specimens and there was not any distinction between relative deformations of sand particles and fiber.

As the macroscopic experiments focused on elastic wave propagation, all the grain-scale tests were performed in the normal direction (i.e., we didn’t focus in the present study on the shearing behavior of sand-fiber contacts). This is because we would expect a stronger influence of the normal contact response from the microscopic tests on the wave propagation parameters compared with the respective influence of the tangential – load (frictional) response [36].

In total twelve samples were prepared and tested for the micromechanical tests; six specimens of LBS grains and six specimens of Blue sand grains (three samples from each sand with fibers at their contacts and also three samples from each material without fibers). Note that these experiments provided some qualitative insights to enrich the macroscopic observations, and that it was not intended to provide a direct quantitative correlation between fiber amount in the grain-scale tests with that in the macroscopic experiments. In the subsequent sections, the grain-scale test results are recalled, particularly in the discussion on the influence of fiber inclusion on the wave propagation parameters of the specimens as the analysis of the influence of grain-scale parameters in stiffness anisotropy is not technically feasible to be analyzed based on the present experimental methods. Micro-CT Xray tomography, similar to the studies by [56, 73] on binary granular systems could be a more adequate approach to study the role of microscopic parameters on stiffness anisotropy in future studies and perhaps the potentially important role of fiber orientation.

3. Results and discussions

3.1 Signal analysis and interpretation of measured wave velocities and respective estimation of elastic stiffness

To quantify the effect of fibers on elastic wave propagation and stiffness (G_{max}) of the mixtures, bender element (BE) tests were carried out on binary sand-fiber specimens using a range of fiber contents. Representative plots of the transmitted and received shear waves from the BE tests are shown in Figure 7 (note: these results correspond to real measurements of raw data and the vertical axis in Figure 7 is expressed in voltage units, where the input signal had an amplitude of 14V). The two methods used in the study to interpret the output signal to estimate shear wave velocities were the first time of arrival (denoted as FT) method and the peak-to-peak time of arrival (denoted as PP) method. Both of these methods have been discussed and evaluated in previous works [20, 76-77]. Shear wave velocities (V_s) measured from the FT and PP methods in the present work provided very small differences within a range of ±5% and a comparison of the data based on these two methods for the whole set of data is given in Figure 8. In the subsequent discussions, the PP method is used to examine the wave velocity and stiffness parameters of the binary specimens.

Youn et al. [78] have suggested that the total mass density should not be used to convert V_s to G_{max} for saturated sands because of the dispersion characteristics, as the BE is a high frequency method and thus, relative movement between solid grains and water occurs during the excitation of the specimen. Therefore, the dispersion and attenuation of the elastic wave propagation through fluid-saturated soils can be considered in terms of the Biot's theory [79-80]. This theory considers the applied input frequency of the excitation, the density of the solid grains and the fluid and also the permeability of the material. Correction of the density of the specimen is therefore performed mostly for highly permeable materials. In this study, G_{max} values were computed from the equivalent density which provides much better matching of the results between RC and BE tests [18, 20]. A basic assumption in the present study was that the solid skeleton of the specimens is composed of both sand particles and fiber inclusion.

In specific, based on Youn et al. [78], the following expression was used to estimate the elastic stiffness from the BE tests:

$$G_{max} = \rho_{eq} \times (V_s)^2 = \left[(1-n) \times \rho_g + \left(1 - \frac{1}{a}\right) \times n \times \rho_f\right] \times (V_s)^2 \qquad (1)$$

where (ρ_{eq}) is the equivalent density, (n) is the porosity, (ρ_g) and (ρ_f) are the mass density of the solid grains and the fluid, respectively, and (a) is a constant which ranges between 2 and 3 [78, 81]. In the present study, similar to Li and Senetakis [18], a value of a=2 was adopted.

A comparison of the G_{max} values from the BE tests and the RC tests using bulk density (i.e., traditional approach) and equivalent density (i.e., Biot's theory) is given in Figure 9. These data suggest a much closer estimation of the elastic stiffness from the BE tests with that of the RC tests when the equivalent density is used. Thus, for further interpretations and data analysis from the bender element tests, the method proposed by Youn et al. [78] based on Biot's theory is adopted in the study. It is noticed, however, that for the resonant column tests, as they are low-to-medium frequency experiments, bulk density is used to estimate elastic stiffness.

3.2 Stiffness and stiffness anisotropy of isotropically consolidated fiber-sand mixtures

3.2.1 Macroscopic observations

The impact of fiber content on G_{max} of the isotropically consolidated specimens is illustrated through representative plots in Figures 10 and 11 in terms of stiffness – pressure and in Supplementary Figure 3 in terms of shear wave velocity – pressure relationship. For each fiber content, two samples were prepared to assess the reproducibility of the test results. To exclude the effect of void ratio, G_{max} values (as well as V_s values in Supplementary Figure 3) obtained from the BE tests are normalized with respect to a commonly used void ratio function $f(e)=e^{-1.3}$ [82]. Plots of normalized stiffness against the normalized pressure are given in Figure 10(a) and Figure 11(a). Figure 10(a) indicates that the addition of fibers tends to decrease $G_{max(hv)}$, however, it has a positive effect on $G_{max(hh)}$ after eliminating the effect of void ratio as shown in Figure 11(a). $G_{max(vh)}$ also reduced with an increase of the fiber content as presented by [18, 20]. Other void ratio functions (for example the expression proposed by Hardin and Black [83]) were used to analyze the data, and the same conclusions were drawn that the inclusion of fibers results in a decrease of $G_{max(vh)}$ and $G_{max(hv)}$ and an increase of $G_{max(hh)}$. The data of Figures 10(a) and 11(a) are reproduced in Supplementary Figures 3(a) and 3(b), respectively, in terms of shear wave velocity against the normalized pressure. The results from these plots provide very similar qualitative conclusions between stiffness and wave velocity analyses, and thus, for further interpretations and description of the model parameters, stiffness (G_{max}) is chosen in the present study.

The granular void ratio (e_{gr}) was also adopted to quantify the impact of fiber content (FC) on the elastic stiffness of the binary samples. In the granular void ratio, the volume of fibers is considered as part of the volume of voids and the solid skeleton consists of the volume of sand grains. $G_{max(hv)}$ and $G_{max(hh)}$ normalized with respect to $F(e_{gr})$ are plotted in Figure 10(b) and Figure 11(b), respectively. However, the use of the granular void ratio is ineffective to eliminate the effect of fiber content. It is seen in these figures that even after the normalization of G_{max} with respect to the granular void ratio of the specimens, the drop of $G_{max(hv)}$ and the increase of $G_{max(hh)}$ with the increase of fiber content is still consistent with the results presented in Figures 10(a) and 11(a). Therefore, the conventional void ratio (e) was used for the subsequent analysis as it is commonly used in the literature.

To examine the impact of fiber content on elastic stiffness, power-law type expressions were fitted to the experimental data (Figures 10(a) and 11(a)) using the general expression of Eq. (2), which is a semi-analytical formula used in the analysis of elastic stiffness in granular materials [25, 84]:

$$G_{max} = A_G \times e^{-1.3} \times \left(\frac{p'}{p_a}\right)^{n_G} \tag{2}$$

Using the least square error approach, the best fit parameters A_G and n_G for each specimen have been obtained and depicted in Figures 12(a) and 12(b) against the content of fibers (FC). These data suggest that both $A_{G(vh)}$ and $A_{G(hv)}$ decrease with increasing FC. In contrast, $A_{G(hh)}$ is slightly increased when fiber content increases. It is also noted that the resultant model parameters $A_{G(vh)}$, $A_{G(hv)}$ and $A_{G(hh)}$ are approximately the same for pure sand specimens and given that the n_G values are very close at FC=0%, it is implied that pure sand specimens have isotropic stiffness.

The presence of fibers leads to an increase of $G_{max(hh)}$ and a decrease of $G_{max(vh)}$ and $G_{max(hv)}$, where $G_{max(vh)}=G_{max(hv)}$. As for the power n_G, no clear trend could be found based on the data presented in Figure 12(b). It has been demonstrated in the literature [7] that the nonlinear trend of parameters could be normalized as a linear function. Therefore, the power n_G was further normalized to the values of initial dry density γ_d and fiber content as:

$$n'_G = \log\left(\frac{n_G}{\gamma_d}\right) \times (1 + FC) = -1.37 \times FC - 1.53 \tag{3}$$

The normalized power n'_G correlates well with the content of the fibers as shown in Figure 12(c). It is noted that the normalized power n'_G obtained from G_{vh}, G_{hv} and G_{hh} follows a relatively similar linear trend. Therefore, one linear correlation between all normalized n'_G values and fiber contents could be applied in the interest of simplicity. Subsequently, the value of the power n_G is positively correlated with initial dry density and fiber content.

One possible explanation on the increase in stiffness in the horizontal direction when fibers are added in the sand is that fibers are, predominantly, horizontally oriented in the mixtures due to the specimen preparation method adopted. This has also been supported by other researchers who used similar techniques as discussed in section 2.2 [55-57, 69]. The horizontal layer structure results in more sand-sand ("rigid") contacts being replaced by the softer sand-fiber-sand ("rigid-soft") contacts in the vertical direction than in the horizontal direction. The shear wave velocity is reduced at the contacts of the particles [25, 85], therefore the wave transmits faster in the horizontal direction. There are also examples in the literature which show that a horizontal layering structure results in a greater value of $G_{max(hh)}$ under isotropic loading. For example, for reconstituted and intact clays, Kuwano [85] reported that G_{hh} was in general greater than G_{vh}. They suggested that the elongated/flaky particles of the clay tend to be oriented in the horizontal direction, which results in more contacts being formed during deposition in the vertical direction than in the horizontal direction. Assuming that attenuation of wave velocity takes place, predominantly, at the contacts of the particles, the wave transmits faster in the horizontal direction. Ng and Leung [86] have demonstrated that the measured shear wave velocity in the horizontal plane ($V_{s(hh)}$) of completely decomposed tuff (CDT), which is a type of clastic material caused by the weathering of the parent rock, is consistently higher than the velocities in the other two directions ($V_{s(hv)}$ and $V_{s(vh)}$) for samples subjected to an isotropic stress state. They concluded from soaking tests that CDT has a horizontal layering structure. Shear waves transmitted horizontally with a horizontal polarization travel along a relatively stiffer horizontal layer (hh plane), resulting in a higher shear-wave velocity $V_{s(hh)}$ compared with $V_{s(hv)}$ and $V_{s(vh)}$.

Similar trends could also be observed for Sydney sand-fiber mixtures and representative results from this group of tests are given in Figure 13. It can be seen that model parameters $A_{G(vh)}$, $A_{G(hv)}$ and $A_{G(hh)}$ are approximately the same in magnitude for pure Sydney sand specimens as for the BS1 sand. The presence of fibers leads to a decrease of $G_{max(vh)}$ and $G_{max(hv)}$, and they are equal in magnitude. However, the effect of fibers on $A_{G(hh)}$ is relatively small. For instance, $A_{G(hh)}$ for SS reinforced with 1% fibers is approximately the same as for the unreinforced specimen, and similarly, $A_{G(hh)}$ for BS2 mixed with 1% fibers is at the same level as that of the pure sand specimen (Figure 13), which is a completely different observation compared with BS1-fiber mixtures. This is speculated to be because of the very different gradings and particle shapes between these three types of sands. It is therefore understood that the impact of fiber inclusion on the wave propagation and elastic stiffness in different directions depends on the grain size distribution characteristics and particle shape of the host sand. As it was discussed in section 2.1, Sydney sand (SS) is a uniform natural sand of fairly regular-in-shape grains, BS1 is a well-graded sand of irregular-in-shape grains and BS2 is a uniform material with irregularly shaped particles.

3.2.2 Microscopic observations

The decrease of elastic stiffness (G_{vh}, G_{hv}) because of the increased contacts of sand-fiber-sand in the vertical direction, can be also explained, partly, by the inference of the polypropylene fibers, as a softer material, in reducing the normal contact stiffness of the interfaces. In this case, we assume that G_{max} is influenced, predominantly, by the normal contact response of the interacting grains as the contact mechanics theories would imply (after [25, 84]). This assumption was also confirmed in the recent numerical study by Reddy et al. [36] in the analysis of the small-to-medium strain stiffness of granular materials. In specific, one of the key plots from the study by [36], is given in Figure 14 which shows, based on discrete element simulations, the relative contribution of shear and normal contact forces of a granular assembly (pure sand) for a minute increment of the deviatoric stress (at this small increment of the deviatoric stress, G_{max} was defined by Reddy et al. [36]). This plot shows that the shear force contribution is, approximately, only 10% to 20% of the normal force counterpart, demonstrating the dominant influence of the normal contact response rather than the tangential contact response in the multi-scale analysis of the macroscopic small-strain stiffness.

Recalling the micromechanical experiments on sand-sand contacts in the presence of fibers and implementing Hertz contact model to quantify the normal load – displacements curves, shows that the presence of fibers decreases the normal contact stiffness.

Figure 15 provides a representative example in applying Hertz fitting to the experimental data and also gives an illustration of the parameters used in the analytical expression, which is given as:

$$F_N = \frac{4 \times (R^*)^{\frac{1}{2}} \times E^* \times \delta_N^{\frac{3}{2}}}{3} \tag{4a}$$

$$\frac{1}{R^*} = \frac{1}{R_1} + \frac{1}{R_2} \tag{4b}$$

In Equation (4), F_N is the normal load, δ_N is the normal displacement, R^* accounts for the equivalent radius given from Equation 4(b), in which R_1 and R_2 represent the radius of the two particles in contact, and E^* is the equivalent or contact Young's modulus. In the fitting process, similar to the descriptions by Ren et al. [38], MATLAB optimization toolbox was used to assess the best-fitted parameters of the theoretical model (in which case E^* is the fitting parameter).

The normal load – displacement curves of the different samples from the grain-scale experiments are given in Figure 16. In this figure, the range of E^* values (equivalent or contact modulus) based on Hertz fitting for each type of contact is displayed. It is noticed that the LBS grain contacts have much higher E^* values compared with the Blue sand (E^* ~ 11.0-19.2 GPa for LBS and 2.4-5.5 GPa for BS), signifying greater normal contact stiffness. This is also confirmed by the much steeper part of the curves at larger displacements, where the relationship between normal load (or normal contact force) and displacement becomes almost linear (beyond the initial regime of non-linear increase of the load). This behavior, as also discussed by Tian et al. [66], is related with the much smoother surfaces of the LBS grains leading to higher normal contact stiffness during the virgin loading of the particle contacts. Perhaps, the differences in the normal loading behavior between LBS and Blue sand grain contacts can also explain, partly, the higher sensitivity of the elastic stiffness to the confining pressure for the Blue sand as the macroscopic test results by Payan et al. [64] would suggest. This is because the Blue sand displays a softer contact response, thus leading to greater fabric changes during the elevation of the confining pressure. It is implied from these discussions that the morphologies of the particles at different scales play their own role in assessing the elastic stiffness – pressure relationship, which involves both mesoscopic grain morphology (i.e., particle shape) and microscopic particle morphology (i.e., roughness), as also previous works have suggested [64, 87].

Despite these differences between the pure sand grain contacts, the behavior is relatively homogenized when fibers are added as shown in Figures 16(b) and 16(c), in which case the Hertz analysis shows a reduction of contact modulus of approximately one order of magnitude (~5 to 10 times) for sand-fiber specimens compared with pure sand grain contacts. This significant drop in contact stiffness is because the system of sand-fibers behaves similar to "rigid-soft" systems as also described in previous studies on sand particle – polymeric material interfaces [66]. A theoretical illustration on the influence of soft synthetic (polymeric) inclusions at the contacts of sand grains is given in Figure 17. Because of the softer and visco-elastic behavior of synthetic inclusions, apart from their contribution in altering the normal contact response of the interfaces within the granular system, also cause increased energy dissipation as the multi-scale test results by Li et al. [42] showed on sand-fiber composites. In specific, the study by [42] focused on measurements of material damping at the macroscopic level through resonant column tests, and the grain-scale response of the interfaces (in the tangential direction) at the small scale through microscopic experiments. This visco-elastic behavior and significant energy dissipation at the interfaces was also supported by the micromechanical tests of Tian et al. [66] on elastomer-sand grain contacts. Additionally, the study by [66] showed that for brittle to elastoplastic materials such as sand grain contacts, the behavior during particle perturbations at small levels of displacements may be elastic (for spherical and relatively smooth quartz grains), or elastoplastic (for irregular-in-shape with rougher textures sand grains). However, plastic-induced strains majorly result from surface damage of micro-asperities.

For composite interfaces (rigid-soft contacts) with the inclusion of polymeric-based materials, the behavior is highly hysteretic, resulting in a significant dissipation of energy. An illustration of these different types of normal contact behavior as reported by Tian et al. [66] (re-drawn by the authors), is given in Figure 18. An additional observation from the micromechanical response of the sand-fiber samples in the present study (Figure 16(d)), which was also discussed on sand-granulated elastomer contacts by [66], is that despite the significant decrease of the normal contact stiffness when synthetic inclusions interact with sand grains, the specimens resemble, partly, some influence of the sand type. As shown in Figure 16(d), despite the inter-test variations, the sand-fiber contacts with LBS particles have slightly greater contact modulus values (and also normal stiffness values) compared with that of Blue sand particles (~ 0.8-2.7 GPa for LBS-fiber against 0.4-1.2 GPa for BS-fiber). This can possibly explain the observations and model development by Li et al. [20] on the elastic stiffness of sand-fiber mixtures subjected to isotropic loading. In that study it was shown that the properties of the host sand resemble an influence in the model development, i.e., elastic wave propagation parameters are given as a function of both fiber content and host sand characteristics. This can be explained, partly, by the influence of sand type on the response of the sand-fiber contacts (despite some trend to homogenization).

3.3 Stress induced anisotropy

To investigate the influence of the anisotropic stress state on the elastic wave propagation and stiffness anisotropy of fiber-sand mixtures, several tests were performed applying different stress paths over a wide range of stress ratios (Table 3, Figure 5). The $G_{max(vh)}$ and $G_{max(hh)}$ values under anisotropic loading paths are plotted against the stress ratio in Figure 19. To remove the effect of volume change and variations in void ratio on the stiffness of the specimens subjected to anisotropic stress state, the values of G_{max} obtained from the test results at each deviatoric stress were normalized with respect to the void ratio function in Figure 19(a). The effect of stress anisotropy was captured through the ratio of the normalized stiffness under isotropic and anisotropic stress states, $G_{max,normalized} = [G_{max\ (ani)}/\ F(e_{ani})]/[G_{max\ (iso)}/F(e_{iso})]$ in Figure 19(b).

In triaxial compression where the radial stress is smaller compared with the deviatoric stress but p' is kept constant, $G_{max(vh)}$ increased, while $G_{max(hh)}$ decreased, with the change of stress ratio for both reinforced and unreinforced specimens, as can be seen in Figure 19(a). For the unreinforced specimens, $G_{max(vh)}$ was found to be greater than $G_{max(hh)}$ under the same stress state. Jardine et al. [88] explained that the shear waves are unlikely to pass through the soil mass evenly. It was stated in that work that it is far more probable that the shear waves travel mainly through the network of the most highly stressed (and therefore stiffest) force chains, with the particles' equilibrium being satisfied by complex interactions with their neighbors, rather than the simple system of complimentary shear stresses implicit in elastic body wave theory. From results using the discrete element method (DEM) on spherical particles by Jardine et al. [88], it was demonstrated that the strongest force chains line up with the vertical direction under anisotropic stresses, which leads to relatively higher values of $V_{s(vh)}$. Similarly, Gu et al. [89] demonstrated from DEM analyses that the distribution of contacts among the grains remains almost unchanged in the vertical direction under anisotropic loading, and that contact forces are re-distributed, primarily, to resist the external anisotropic load which leads to an increase of $G_{max(vh)}$. On the contrary, for the composite granular materials tested in the current study, all the data points of $G_{max(vh)}$ are located well below the corresponding data of $G_{max(hh)}$, which is hypothesized to be caused by the orientation of the fibers as discussed in the previous sections.

To study the exclusive impact of stress anisotropy on G_{max} removing possible influence of different void ratios between different specimens, a normalized expression of stiffness, as introduced by Payan et al. [90] and Senetakis and Li [91] for pure sands and fiber-reinforced sands, respectively, was adopted. Based on this concept, the data from Figure 19(a) are reproduced in Figure 19(b), where the values of the vertical axis are normalized with respect to a void ratio function. These plots suggest that the increase of normalized $G_{max(vh)}$ as the stress ratio increases is more pronouncedly observed for the softer fiber-reinforced specimens with smaller $G_{max(vh)}$ values than the stiffer unreinforced specimens. For a fiber content equal to 2% at p' = 100 kPa, $G_{max,normalized}$ showed an increase of the order of 30%, approximately, while an increase of 10%, approximately, can be observed for the pure sand specimen with the change of stress ratio from 0 to 1. It is shown from Figure 19(b) that the effect of stress anisotropy is markedly more pronounced for the mixtures of the well-graded and of angular grains crushed rock compared with the mixtures of the uniform and of sub-rounded grains natural (Sydney) sand. It is noticed that Sydney sand has a greater $G_{max(vh)}$ value and the structural stability and non-homogeneous distribution of the contact normal forces among the particles of the tested sands due to shearing might be the reason for the different sensitivities of different specimens under stress anisotropy [90]. This is also very likely to be caused by the higher normal contact stiffness of the natural sand grain contacts compared with that of Blue sand grain contacts, as the grain-scale tests suggested, providing a strong link between the microscopic observations from the grain-scale tests with the macroscopic test results in the present study. In this case, we make the assumption that it is more probable the Sydney sand grains to have a much more similar contact stiffness with LBS, compared to that of Blue sand, based on the local morphology, surface roughness and origin among the different materials [39, 66, 68, 92-93].

Measurements of stiffness when applying and removing stress anisotropy suggested that the properties of the host sand have a significant influence on the measured stiffness between the loading and unloading paths. For instance, $G_{max(vh)}$ for the natural Sydney sand during the removal of the stress anisotropy is almost the same as in the loading process, which agrees with the observations by [54]. However, $G_{max(vh)}$ for BS1 during the unloading process is slightly higher compared to the loading process, while the $G_{max(vh)}$ for BS1 mixed with 2% fibers at q/p'+1=1 during the unloading process is 25% higher than that of the loading process. This is because during the application of the deviatoric stress, plastic shear strains were induced in the specimens of BS1 and BS1-fiber mixtures, which, due to the angular and rough grains of the crushed rock, resulted in greater compressibility compared with the specimens composed of Sydney sand. To further investigate the stiffness anisotropy as a result of induced strains, four representative specimens (no. 28, 30, 32 and 34 from Table 3) were analyzed. The ratio of $G_{max(vh)}$ at the anisotropic consolidation state (q/p'>0) over $G_{max(vh)}$ at the isotropic consolidation state (q/p'=0) of these four specimens is plotted against the shear strain in Figure 20(a). In this figure, the black continuous line stands for the fitting curve from the data analysis, representing an “average” increase of the stiffness (from isotropic to anisotropic state) with increasing induced shear strains. A relatively good correlation could be established, which indicates that the differences in the behavior of pure

BS1 and BS1 with fibers under triaxial compression is contributed, partly, by the induced shear strains.

It is noticed that the current study aims to explore in a qualitative way the different responses of various granular materials (including sand-fiber composites) under stress anisotropy following a constant p' path rather than developing a correlation between shear strain and the ratio of $G_{max(ani)}$/ $G_{max(iso)}$, therefore, the equation and the coefficient of determination are not displayed. Based on published data by Senetakis and Li [91], a comprehensive database of a series of triaxial compression tests at different effective confining stresses on BS1 with different fiber contents were re-analyzed in a similar way as the analysis presented in Figure 20(a). These data are given in Figure 21, and similar to Figure 20(a), the black continuous line stands for the fitting curve from the data analysis. Though some scatter in the data is acknowledged, there is a clear influence of the induced plastic strains on the ratio of $G_{max(ani)}$/$G_{max(iso)}$. In Figure 20(b) the ratios of $G_{max(vh)}$ at the unloading stage over $G_{max(vh)}$ at the loading stage for sands and sand-fiber mixtures are plotted against the shear strain. The data indicate that for BS1 and BS1 with fibers, a portion of the total strain is plastic and that $G_{max(vh)}$ values are greater at the unloading stage, while for SS the shear strain is almost recovered completely and $G_{max(vh)}$ values are almost identical during the loading and unloading stages. During the unloading process, the effect of stress ratio is almost negligible, as can be observed from the data in Figure 19(a) where the red-colored trend line is nearly flat. Therefore, the different trends observed for various specimens with respect to the sensitivity of stiffness to the stress ratio is related, solely, to the induced shear strains. The results in Figure 19(a) also show that the values of $G_{max(hh)}$ decrease with the increase of stress ratio for both unreinforced and reinforced specimens and that the presence of fibers seems to slow down the change of $G_{max(hh)}$ with the increase of stress ratio. A similar analysis correlating $G_{max(hh)}$ with shear strain was conducted, however the correlation between $G_{max(hh,ani)}/G_{max(hh,iso)}$ and shear strain was found to be relatively weak. Based on this, a clear conclusion could not be drawn on the influence of fiber content on $G_{max(hh)}$ under anisotropic stress state. These results, along with what the literature on geosynthetics has suggested [57, 94-95], would necessitate more in-depth analysis of the involved micromechanisms with respect to fiber content and geometric arrangement to be performed in future studies. For example, the role of mobilized friction was not examined explicitly in this study which could play some important role on the behavior of the anisotropically loaded specimens.

3.4 Stiffness anisotropy of sand and sand-fiber mixtures under extension and compression stress paths

To examine further the stiffness anisotropy of sand-fiber composites subjected to stress anisotropy, six additional samples were constructed with different fiber contents and were subjected to triaxial extension and compression stress paths. The stiffness ratio defined as $[G_{max(hv)}/F(e)]/[G_{max(hh)}/F(e)]$ is plotted against the stress ratio in Figure 22. At the isotropic stress state, the stiffness ratio is approximately equal to 1 for pure sand, while the ratio decreased to 0.77 when 1% fibers were added. Based on these results, the data points of the sand-fiber mixtures are located parallel and below of that of the pure sands, with a drop of the stiffness ratio of, approximately, 20% when the fiber content increased from 0% to 1%. Another observed pattern is that the stiffness ratio increased with the increase of stress ratio for both sand-fiber mixtures and pure sand specimens. For example, stiffness ratio for sand mixed with 1% fibers is about 0.77 when $q/p'=0$, while this value increased to about 1 when $q/p'=1$. These data suggest that the addition of fibers forms an anisotropic fabric when the specimen is subjected to an isotropic stress state, however the induced shear strains due to stress anisotropy play a homogenizing role. The stiffness ratios between loading and unloading processes were found to be almost identical.

3.5 Discussion on practical applications

Although in-situ stress conditions are usually anisotropic, it is reasonable to assume that small strain shear modulus (G_{max}) obtained under anisotropic stress conditions approximately equals to that under isotropic conditions for geo-materials that are less sensitive to k_0 conditions. The measurement of shear wave velocities and elastic stiffness through isotropically consolidated specimens allows the quantification of the effect of the structural anisotropy, which is very important to be obtained so that to understand fundamental mechanisms of granular materials and reinforced soils with fibers. Elastic stiffness of geo-materials and geosynthetics is a key design parameter in many applications such as earthquake ground response analysis, analysis of vibrations due to machine foundations, and the prediction of deformations of foundations and geo-systems. In addition, the knowledge of the stiffness in different directions is important in design, for example in the analysis of earth retaining structures, vertical cuts or slopes, embankments, deep excavations, deep and shallow foundations, and tunneling. Simpson et al. [96] demonstrated that the values of G_{vh} and G_{hv} of London clay were approximately the same at all depths but the values of G_{hh} were significantly larger. They showed that the degree of anisotropy G_{vh}/G_{hh} was of the order of 0.65 based on measurements on specimens subjected to isotropic consolidation. Additionally, the study by [96] incorporated this degree of structural anisotropy into a non-linear finite element analysis to study settlements induced by tunnel construction, which corresponded well with the field observations of surface settlements (application refers to Heathrow Express trial tunnel). The numerical analyses of ground movements above tunnels overlook the effect of stiffness anisotropy and often give settlement troughs which are much wider than those observed in practice. Similar to (inherently anisotropic) clays, the fiber-sand granular composites examined in the current study display greater values of G_{hh}. Therefore, the effect of this structural anisotropy of fiber-sand mixtures should be taken into account when elasticity-theory-based methods are adopted to predict foundation settlements. Consideration of stiffness anisotropy is also important to be encountered for fiber-reinforced sands, as the results of the study showed that the fiber inclusion had a different contribution to the stiffness in different directions.

4. Conclusions

A total of 38 specimens were tested in a Hardin type resonant column equipped with vertical bender elements and a stress path triaxial apparatus equipped with lateral bender elements. Three types of sands with different gradings or particle shapes were selected as host sands. Polypropylene fibers were used to examine the effect of fiber content on the elastic stiffness. The stiffness anisotropy of sand-fiber mixtures under isotropic or anisotropic loading stress paths was comprehensively studied, even though the present data have an inherent influence of the formed fabric based on the adopted sample preparation method, which results in preferable horizontal orientation of the fibers. The main findings of this study can be summarized as follows:

1. Sands exhibit stiffness isotropy under isotropic stress state so that $G_{max(vh)}$, $G_{max(hv)}$ and $G_{max(hh)}$ are equal in magnitude. Their absolute values depend, predominantly, on the characteristics of the sand in terms of coefficient of uniformity and particle shape/morphology.

2. The addition of fibers leads to a decrease of $G_{max(vh)}$ and $G_{max(hv)}$, while the two moduli with subscripts “vh” and “hv” are found to be equal (the subscripts describe the direction of wave propagation and particle motion). Micromechanical-based experimental results showed that the

normal contact stiffness of the sand grain contacts decreases when fibers are added, which can partly explain the macroscopic observations. However, the grain-scale tests showed that the sand type resembles an influence on the contact response of the sand-fiber specimens. This observation can provide some additional support to previous studies which developed stiffness expressions for sand-fiber binary materials suggesting that the sand type resembles an influence on the wave propagation parameters of these binary materials. This observation may also have implications in DEM modeling of binary systems, as the input contact properties would depend not only on the presence of the softer polymeric inclusion, but also the type of the granular material that is targeted to be modeled.

3. The presence of fibers results in an increase of $G_{max(hh)}$ compared with the value of $G_{max(vh)}$ = $G_{max(hv)}$ for the well-graded host sand (Blue sand 1), however, this effect is almost negligible for uniform Blue sand 2 and Sydney sand. It is understood that the influence of fiber inclusion on stiffness anisotropy is dependent on the type of the host sand and its grain size characteristics. This outcome would worth further investigation in future studies, for example by performing DEM or micro-CT tomography analysis which can help to provide some further understanding on the micromechanisms which are contributed by the type of the sand, particularly the role of grading characteristics. Despite this, in FEM analyses of soil-foundation interaction problems, where a stiffness matrix is needed as input model, this anisotropic behavior should be taken into account, especially for fiber-reinforced soils which consist of well-graded host geo-material. Future studies could also be directed in the analysis of the problem by constructing specimens with different sample preparation methods. For example, the orientation of the fibers could be a key in modeling small-strain stiffness and understanding the anisotropic nature of sand-fiber systems.

4. For the specimens subjected to stress anisotropy, it was found that $G_{max(vh)} \neq G_{max(hv)} \neq G_{max(hh)}$. and also the increase of stress ratio leads to an increase of stiffness anisotropy. Additionally, the inclusion of fibers tends to change the stiffness anisotropy of the mixtures; in particular, the higher the fiber content, the more pronounced the effect of fiber inclusion on stiffness anisotropy. Thus, for the investigation of the behavior of binary composite granular materials subjected to stress anisotropy, quantification of the stiffness in one direction (e.g., G_{vh} as commonly obtained in laboratory tests) is not enough to provide complete constitutive modeling. The micromechanisms of this behavior could be further investigated in future works, for example by implementing DEM analyses so that to obtain insights into the competitive mechanisms which lead to stiffness anisotropy.

Acknowledgments

The work was supported by a grant from the Research Grants Council of the Hong Kong Special Administrative Region, China, project no. "CityU 11210419".

Compliance with ethical standards

The authors declare no conflict of interest from the present study. This work contains original material as a result of purely academic study without any kind of private funding or other conflict of interest.

References

1. Michałowski, R.L. & Zhao, A. (1996). Failure of fiber-reinforced granular soils. J. Geotech. Eng. 122(3): 226–234.

2. Michalowski, R. L. (2008). Limit analysis with anisotropic fibre-reinforced soil. Géotechnique 58**(**6): 489–501.

3. Consoli, N.C., Casagrande, M.D.T. & Coop, M.R. (2007). Performance of a fibre-reinforced sand at large shear strains. Geotechnique 57(9): 751-756.

4. Hejazi S.M., Sheikhzadeh, M., Abtahi S.M.,Zadhoush A., 2012. A simple review of soil reinforcement by using natural and synthetic fibres. Construction and Building Materials, 30, 100-116.

5. Diambra, A., Ibraim, E., Russell, A.R. & Muir Wood, D. (2013). Fibre reinforced sands: from experiments to modelling and beyond. International Journal for Numerical and Analytical Methods in Geomechanics 37(15): 2427–2455.

6. Li, C.L. & Zornberg, J.G. (2013). Mobilization of Reinforcement Forces in Fibre-Reinforced Soil. Journal of Geotechnical and Geoenvironmental Engineering 139(1):107-115.

7. Mirzababaei, M., Mohamed, M., Arulrajah, A., Horpibulsuk, S. & Anggraini, V. (2018). Practical approach to predict the shear strength of fibre-reinforced clay. Geosynthetics International 25 (1): 50-66.

8. Al-Refeai, Talal O. (1991). Behaviour of granular soils reinforced with discrete randomly oriented inclusions. Geotextiles and Geomembranes 10(4): 319–333.

9. Al-Refeai, T. & Al-Suhaibani, A. (1998). Dynamic and static characterization of polypropylene fibre-reinforced dune Sand. Geosynthetics International 5(5): 443-458.

10. Dos Santos, A.P.S., Consoli, N.C. & Baudet, B.A. (2010). The mechanics of fibre-reinforced sand. Géotechnique 60 **(**10): 791–799.

11. Diambra, A., Ibraim, E., Russell, A.R. & Muir Wood, D. (2011). Modelling the undrained response of fibre reinforced sands. Soils and Foundations 51(4): 625–636.

12. Ye, B., Cheng, Z. R., Liu, C., Zhang & Y. D. Lu, P. (2017). Liquefaction resistance of sand reinforced with randomly distributed polypropylene fibres. Geosynthetics International 24(6): 625–636.

13. Ghadr, S. (2020). Effect of grain size on undrained anisotropic behaviour of sand–fibre composite. Transportation Geotechnics 22:100323.

14. Ghadr, S. & Bahadori, H. (2019). Anisotropic behavior of fiber-reinforced sands. Journal of Materials in Civil Engineering 31(11): 04019270.

15. Wood, D.M., Diambra, A. & Ibraim, E. (2016). Fibres and soils: A route towards modelling of root-soil systems. Soils and Foundations 56(5): 765-778.

16. Zhang, X. & Russell, A.R. (2020). Assessing liquefaction resistance of fiber-reinforced sand using a new pore pressure ratio. Journal of Geotechnical and Geoenvironmental Engineering 146(1): 04019125.

17. Heineck, K.S., Coop, M.R. & Consoli, N.C., (2005). Effect of microreinforcement of soils from very small to large shear strains. Geotechnical and Geoenvironmental Engineering, 131, No.8,1024-1033.

18. Li, H., Senetakis, K. (2017). Dynamic properties of polypropylene fibre-reinforced silica quarry sand. Soil Dynamics and Earthquake Engineering 100: 224-232.

19. Li, M., He, H. & Senetakis, K. (2017). Behaviour of carbon fibre-reinforced recycled concrete aggregate. Geosynthetics International 24(5): 480-490.

20. Li, H., Senetakis, K. & Khoshghalb, A. (2019). On the small-strain stiffness of polypropylene fibre-sand mixtures. Geosynthetics International 26(1): 66-80.

21. Maher, M.H. & Woods H.D. (1990). Dynamic response of sand reinforced with randomly distributed fibres. Journal of Geotechnical Engineering 116(7):1116-1131.

22. Vettorelo, P.V. & Clariá, J.J. (2018). Modeling the Fibre Addition Influence on the Small Strain Shear Modulus of Sand. Indian Geotechnical Journal 48(1): 196-204.

23. Ishihara, K. (1996). Soil behaviour in earthquake geotechnics. Clarendon Press; Oxford University Press.

24. Clayton, C. (2011). Stiffness at small strain: Research and practice. Géotechnique 61(1):5-37.

25. Cascante, G. & Santamarina, C. (1996). Interparticle contact behaviour and wave propagation. Journal of Geotechnical Engineering 122(10): 831–839.

26. Gu, X.Q. & Yang, J. (2013). A discrete element analysis of elastic properties of granular materials. Granular Matter 15:139-147.

27. Gu, X., Yang, J. & Huang, M. (2013). DEM simulations of the small strain stiffness of granular soils: effect of stress ratio. Granular Matter 15:287-298.

28. Otsubo, M., O'Sullivan, C., Hanley, K.J., Sim, W.W. (2017). Influence of packing density and stress on the dynamic response of granular materials. Granular Matter, 19, Article Number: 50.

29. Hu, T., Van Gorder, R.A. (2019). Wave propagation and pattern formation in two-dimensional hexagonally-packed granular crystals under various configurations. Granular Matter, 21, Article Number: 3.

30. Wang, C., Zhang, Q., Vavakis, A.F. (2021). Wave transmission in 2D nonlinear granular-solid interfaces, including rotational and frictional effects. Granular Matter, 23, Article Number: 21.

31. O'Donovan, J., Ibrain, E., O'Sullivan, C., Hamlin, S., Muir Wood, D., Marketos, G. (2016). Micromechanics of seismic wave propagation in granular materials. Granular Matter, 18, Article Number: 56.

32. Paulick, M., Morgeneyer, M., Kwade, A. (2015). A new method for the determination of particle contact stiffness. Granular Matter, 17, 83–93.

33. Chung, C.-K., Jang, E.-R., Baek, S.-H., Jung, Y.-H. (2014). How contact stiffness and density determine stress-dependent elastic moduli: a micromechanics approach. Granular Matter, 16, 23-39.

34. Zhou, Z.H., Wang, H.N., Jiang, M.J. (2021). Elastic constants obtained analytically from microscopic features for regularly arranged elliptical particle assembly. Granular Matter, 23, Article Number: 29.

35. Pal, R.K., Awasthi, A.P., Geubelle, P.H. (2013). Wave propagation in elasto-plastic granular systems. Granular Matter, 15, 747-758.

36. Reddy, N.S.C., He, H., Senetakis, K. (2022). DEM analysis of small and small-to-medium strain shear modulus of sands. Computers and Geotechnics, 141, 104518.

37. Yimsiri, S. & Soga, K. (2000). Micromechanics-based stress–strain behaviour of soils at small strains. Geotechnique 50: 559–571.

38. Ren, J., Li, S., He, H., Senetakis K. (2021). The tribological behavior of iron tailing sand grain contacts in dry, water and biopolymer immersed states. Granular Matter, 23(1), 12, https://doi.org/10.1007/s10035-020-01068-0.

39. Sandeep, C.S., Li, S., Senetakis, K. (2021). Scale and surface morphology effects on the micromechanical contact behavior of granular materials. Tribology International, 159, 106929, https://doi.org/10.1016/j.triboint.2021.106929.

40. Taghizadeh, K., Shrivastava, R.K., Luding, S. (2021). Stochastic Model for Energy Propagation in Disordered Granular Chains. Materials, 14, 1815, https://doi.org/10.3390/ma14071815.

41. Tian, Y., Senetakis, K. (2021). Influence of creep on the small-strain stiffness of sand-rubber mixtures. Geotechnique [Ahead of Print] https://doi.org/10.1680/jgeot.20.P.208.

42. Li, H., Kasyap, S.S. & Senetakis, K. (2021). Multi-scale study of the small-strain damping ratio of fiber-sand composites. Polymers, 13(15), 2476.

43. Fatahi, B., Fatahi, B., Le, T.M. & Khabbaz, H., (2013). Small-strain properties of soft clay treated with fibre and cement. Geosynthetics International 20(4): 286-300.

44. Jardine, R. J. (1995). One Perspective of the Pre-Failure Deformation Characteristics of Same Geomaterials. Keynote lecture, Proceedings of International symposium on Pre-failure Deformation of Geomaterials (IS-Hokkaido) 2:855–885.

45. Kuwano, R., Connolly, T.M. & Jardine, R.J. (2000), Anisotropic Stiffness Measurements in a Stress-Path Triaxial Cell. Geotechnical Testing Journal 23(2):141-157.

46. Dutta, T.T., Otsubo, M., Kuwano, R. & Sato, T. (2020). Estimating multidirectional stiffness of soils using planar piezoelectric transducers in a large triaxial apparatus. Soils and Foundations 60: 1269-1286.

47. Zamanian, M., Payan, M., Memarian, S., Senetakis, K. (2021). Impact of bedding plane direction and type of plastic microparticles on stiffness of inherently anisotropic gap-graded soils: Index, wave propagation and micromechanical-based interpretations. Soil Dynamics and Earthquake Engineering [Ahead of Print], https://doi.org/10.1016/j.soildyn.2021.106924.

48. Hendry, M.T., Sharma, J.S., Martin, C.D. & Barbour, S.L. (2012). Effect of fibre content and structure on anisotropic elastic stiffness and shear strength of peat. Canadian Geotechnical Journal 49(4): 403-415.

49. Mitaritonna, G., Amorosi, A. & Cotecchia, F. (2014). Experimental investigation of the evolution of elastic stiffness anisotropy in a clayey soil, Géotechnique 64(6):643-675.

50. Senetakis, K. & He, H. (2017). Dynamic characterization of a biogenic sand with a resonant column of fixed-partly fixed boundary conditions. Soil Dynamics and Earthquake Engineering 95: 180-187.

51. Wang, Y. H. & Gao, Y. (2013). Mechanisms of Aging-Induced Modulus Changes in Sand with Inherent Fabric Anisotropy, Journal of Geotechnical and Geoenvironmental Engineering, 13(9): 470-482.

52. Wang, Y. H. & Mok, C. M. (2008). Mechanisms of Small-Strain Shear-Modulus Anisotropy in Soils, Journal of Geotechnical and Geoenvironmental Engineering 134(10):1516-1530.

53. Zeng, X. & Ni, B. (1999). Stress-induced anisotropic Gmax of sands and its measurement. Journal of Geotechnical and Geoenvironmental Engineering, 125(9): 741–749.

54. He, H., Li, S., Senetakis, K., Coop, M.R. & Liu, S. (2022). Influence of anisotropic stress path and stress history on stiffness of calcareous sands from Western Australia and the Philippines, Journal of Rock Mechanics and Geotechnical Engineering, 14(1), 197-209, https://doi.org/10.1016/j.jrmge.2021.03.015.

55. Diambra, A., Russell, A.R., Ibraim, E. & Muir Wood, D. (2007). Determination of fibre orientation distribution in reinforced sands. Géotechnique 57(7): 623-628.

56. Soriano, I., Ibraim, E., Andò, E., Diambra, A., Laurencin, T., Moro, P. & Viggiani, G. (2017). 3D fibre architecture of fibre-reinforced sand. Granular Matter 19:75, https://doi.org/10.1007/s10035-017-0760-3.

57. Diambra, A., Ibraim, E., Muir Wood, D. & Russell, A.R. (2010). Fibre-reinforced sands: Experiments and modelling. Geotextiles and Geomembranes 28: 238-250.

58. Mandolini, A., Diambra, A. & Ibraim, E., (2019). Strength anisotropy of fibre-reinforced sands under multiaxial loading. Géotechnique 69(3): 203–216.

59. Michalowski, R. L. & Čermákb, J. (2002). Strength anisotropy of fibre-reinforced sand. Computers and Geotechnics 29: 279-299.

60. Krumbein, W. C. & Sloss, L. L. (1963). Stratigraphy and sedimentation. 2nd ed., W. H Freeman and Company.

61. Cho, G. C., Dodds, J. & Santamarina, J. C. (2006). Particle shape effects on packing density, stiffness and strength: natural and crushed sands. Journal of Geoechnical and Geoenvironmental Engineering 132(5): 591-602.

62. Zhou, B., Wang, J. (2017). Generation of a realistic 3D sand assembly using X-ray micro-computed tomography and spherical harmonic-based principal component analysis. International Journal for Numerical and Analytical Methods in Geomechanics, 41(1), 93–109.

63. Zhou, B., Wang, J., Wang, H. (2018). Three-dimensional sphericity, roundness and fractal dimension of sand particles. Geotechnique, 68(1), 18–30.

64. Payan, M., Khoshghalb, A., Senetakis, K. & Khalili, N. (2016). Effect of particle shape and validity of G_{max} models for sand: A critical review and a new expression. Computers and Geotechnics 72: 28-41.

65. Payan M., Senetakis K., Khoshghalb A. & Khalili N. (2016). Influence of particle shape on small-strain material damping of dry sand. Geotechnique 66(7): 610-616.

66. Tian, Y., Kasyap, S.S. & Senetakis, K. (2021). Influence of loading history and soil type on the normal contact behavior of natural sand grain-elastomer composite interfaces. Polymers 13(11):1830.

67. Sandeep C.S. & Senetakis K. (2018). Effect of Young's Modulus and Surface Roughness on the Inter-Particle Friction of Granular Materials. Materials 11:217; doi:10.3390/ma11020217.

68. Ren, J., He, H., Lau, K.-C., Senetakis, K. (2021). Influence of iron oxide coating on the tribological behavior of sand grain contacts. Acta Geotechnica [Ahead of Print], https://doi.org/10.1007/s11440-021-01367-7.

69. Ibraim, E., Diambra, A., Muir Wood, D. & Russell.A.R., (2010). Static liquefaction of fibre-reinforced sand under monotonic loading. Geotextiles and Geomembranes 28(4): 374–385.

70. Li, H., He, H. & Senetakis, K. (2018). Calibration exercise of a Hardin-type resonant column. Géotechnique 68(2): 171–176.

71. He, H. & Senetakis, K. (2016). A study of wave velocities and poisson ratio of recycled concrete aggregate. Soils and Foundations, 56(4): 593-607.

72. Diambra, A. & Ibraim, E. (2015). Fibre-reinforced sand: interaction at the fibre and grain scale. Géotechnique 65(4): 296–308.

73. Cheng, Z.; Wang, J.; Li, W. (2020). The micro-mechanical behaviour of sand–rubber mixtures under shear: An experimental study based on X-ray micro-tomography. Soils Found., 60, 1251–1268.

74. Senetakis, K., Payan, M., Li, H., Zamanian, M. (2021). Nonlinear stiffness and damping characteristics of gravelly crushed rock: Developing generic curves and attempting multi-scale insights. Transportation Geotechnics, 31, 100668, https://doi.org/10.1016/j.trgeo.2021.100668.

75. He, H., Senetakis, K. and Coop, M.R. (2019). An investigation of the effect of shearing velocity on the inter-particle behavior of granular and composite materials with a new micromechanical dynamic testing apparatus. Tribology International, 134, 252-263.

76. Lee, J.S. & Santamarina, J.C. (2005). Bender elements: performance and signal interpretation. Journal of Geotechnical and Geoenvironmental Engineering, 131(9):1063–1070.

77. Leong, E.C., Cahyadi, J. & Rahardjo, H. (2009). Measuring shear and compression wave velocities of soil using bender–extender elements. Canadian Geotechnical Journal 46:792-812.

78. Youn, J.-U., Choo, Y.-W. & Kim, D.S. (2008). Measurement of small strain shear modulus Gmax of dry and saturated sands by bender element, resonant column, and torsional shear tests. Canadian Geotechnical Journal 45(10):1426-1438.

79. Biot, M.A. (1956). Theory of propagation of elastic waves in a fluid-saturated porous solid. I. Low frequency range. Journal of the Acoustical Society of America 28(2): 168–178.

80. Biot, M.A. (1956). Theory of propagation of elastic waves in a fluid-saturated porous solid. II. Higher frequency range. Journal of the Acoustical Society of America 28(2): 179–191.

81. Stoll, R. D. (1979). Experimental studies of attenuation in sediments. Journal of the Acoustical Society of America 63(2): 607–613.

82. Jamiolkowski, M., Leroueil, S. & Lo Priesti, D. (1991). Design parameters from theory to practice. In Proceedings of the international conference on geotechnical engineering for coastal development*:* geo-coast. Coastal Development Institute of Technology Yokohama Japan: 877–917.

83. Hardin, B. O. & Black, W. L. (1966). Sand stiffness under various triaxial stresses. Journal of Soil Mechanics & Foundations Division, ASCE 92(SM2):27-42.

84. Santamarina, C., Klein, K. & Fam, M. (2001). Soils and Waves. John Wiley and Sons, New York.

85. Kuwano, R. (1999). The Stiffness and yielding anisotropy of sand. Ph.D. dissertation. Imperial college, University of London, London, UK.

86. Ng, C. & Leung, E. (2007). Determination of Shear-Wave Velocities and Shear Moduli of Completely Decomposed Tuff. Journal of Geotechnical and Geoenvironmental Engineering 133(6): 630–640.

87. Otsubo, M., O'Sullivan, C. (2018). Experimental and DEM assessment of the stress-dependency of surface roughness effects on shear modulus. Soils and Foundations, 58(3), 602-614.

88. Jardine, R. J., Kuwano, R., Zdravkovic, L., Thornton, C. (1999). Some fundamental aspects of the pre-failure behaviour of granular soils. Proc., Int. Symp. on Prefailure Deformation of Geomaterials, M. Jamiolkowski et al., eds 2:1077–1111.

89. Gu, X., Hu, J., Huang, M., 2017. Anisotropy of elasticity and fabric of granular soils. Granular Matter, 19:33, https://doi.org/10.1007/s10035-017-0717-6.

90. Payan, M., Khoshghalb, A., Senetakis, K. & Khalili, N. (2016). Small-strain stiffness of sand subjected to stress anisotropy, Soil Dynamics and Earthquake Engineering 88:143-151.

91. Senetakis, K. & Li, H. (2017). Influence of stress anisotropy on small-strain stiffness of reinforced sand with polypropylene fibres, Soils and Foundations 57: 1077-1083.

92. Sandeep, C.S., Li, S., Senetakis, K. (2021). Experimental and analytical investigation on the normal contact behavior of natural proppant simulants. Geomechanics and Geophysics for Geo-energy and Geo-Resources, 7: 107, https://doi.org/10.1007/s40948-021-00296-9.

93. Sandeep, C.S, Marzulli, V., Cafaro, F., Senetakis, K., Pöschel, T. (2019). Micromechanical Behavior of DNA-1A Lunar Regolith Simulant in Comparison to Ottawa Sand. Journal of Geophysical Research: Solid Earth, 124(8): 8077-8100.

94. Ziegler, M. (2017). Application of Geogrid Reinforced Constructions: History, Recent and Future Developments, Procedia Engineering, 172, 42-51.

95. Cheng, H., Yamamoto, H., Thoeni, K., Wu, Y. (2017). An analytical solution for geotextile-wrapped soil based on insights from DEM analysis, Geotextiles and Geomembranes, 45, 361-376.

96. Simpson, B., Atkinson, J. H., Jovičić, V. (1996). The influence of anisotropy on calculations of ground settlements above tunnels. Proc. Geotechnical Aspects of Underground Construction in Soft Ground, The City University, London: 591-595.

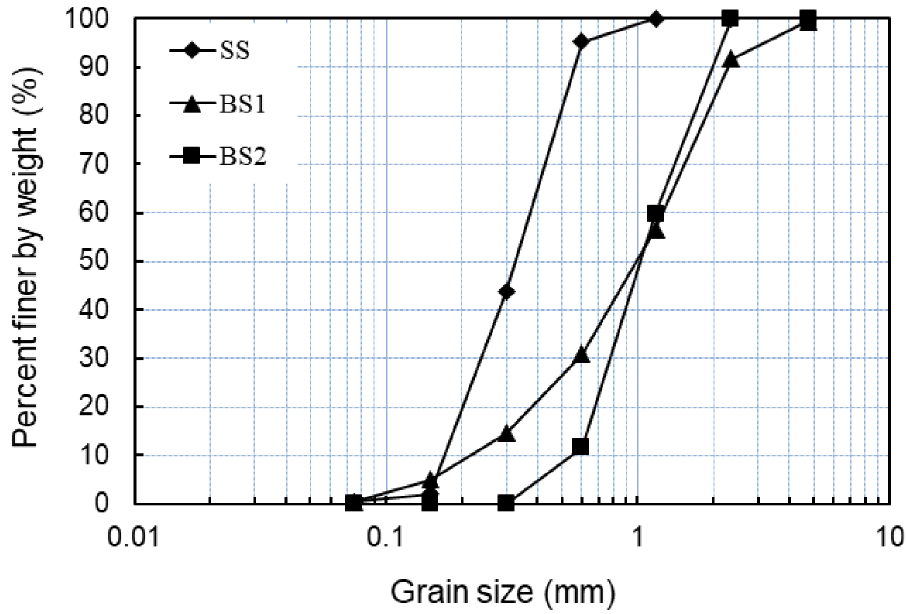

Figure 1. Particle size distribution curves of the host granular materials

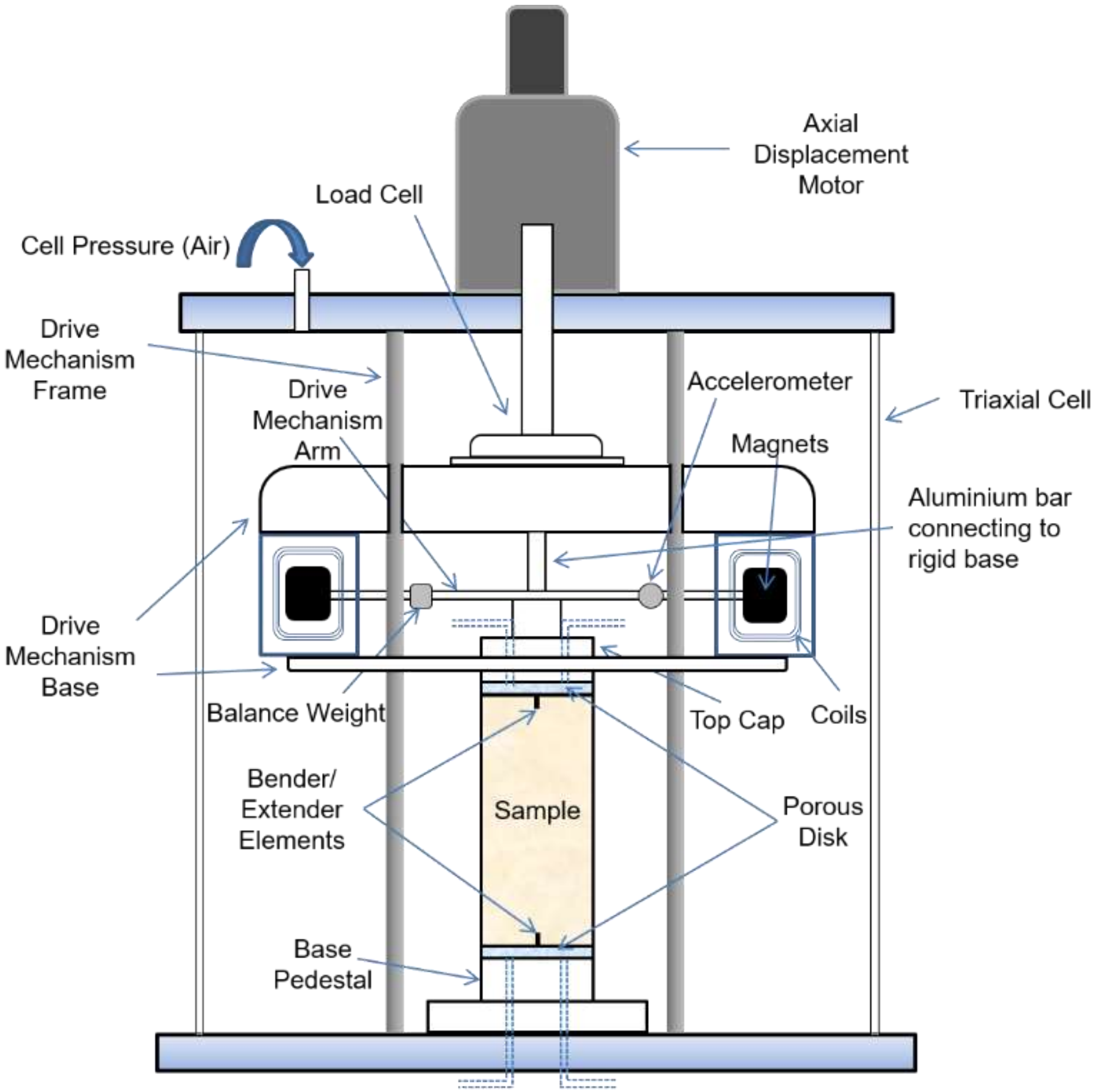

Figure 2. Schematic illustration of Hardin-type resonant column with bender elements instrumentation for the measurements of seismic waves and respective elastic stiffness $G_{max(vh)}$

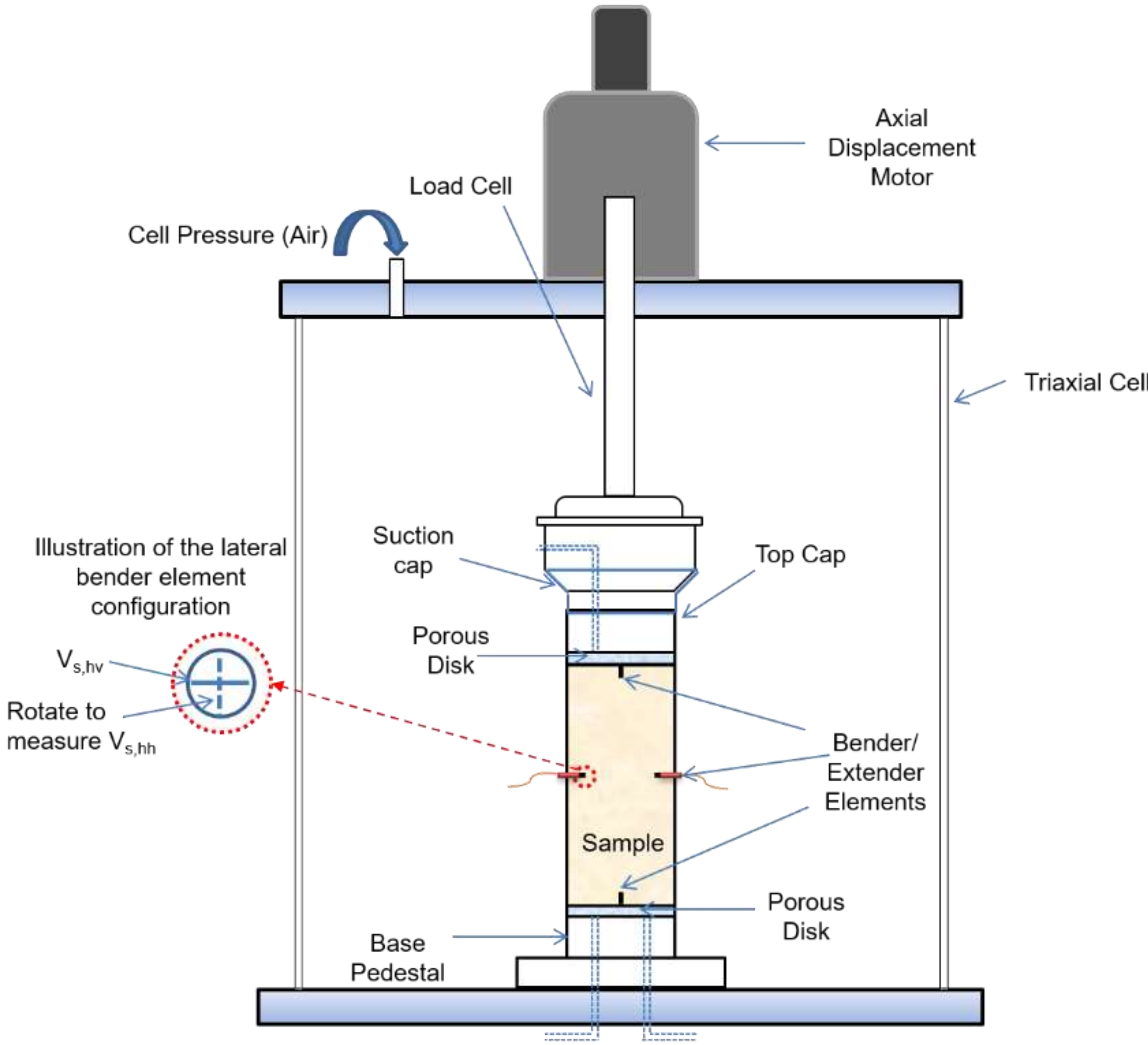

Figure 3. Schematic illustration of stress path triaxial apparatus with bender elements instrumentation for the measurements of seismic waves and respective elastic stiffness $G_{max(hv)}$ and $G_{max(hh)}$

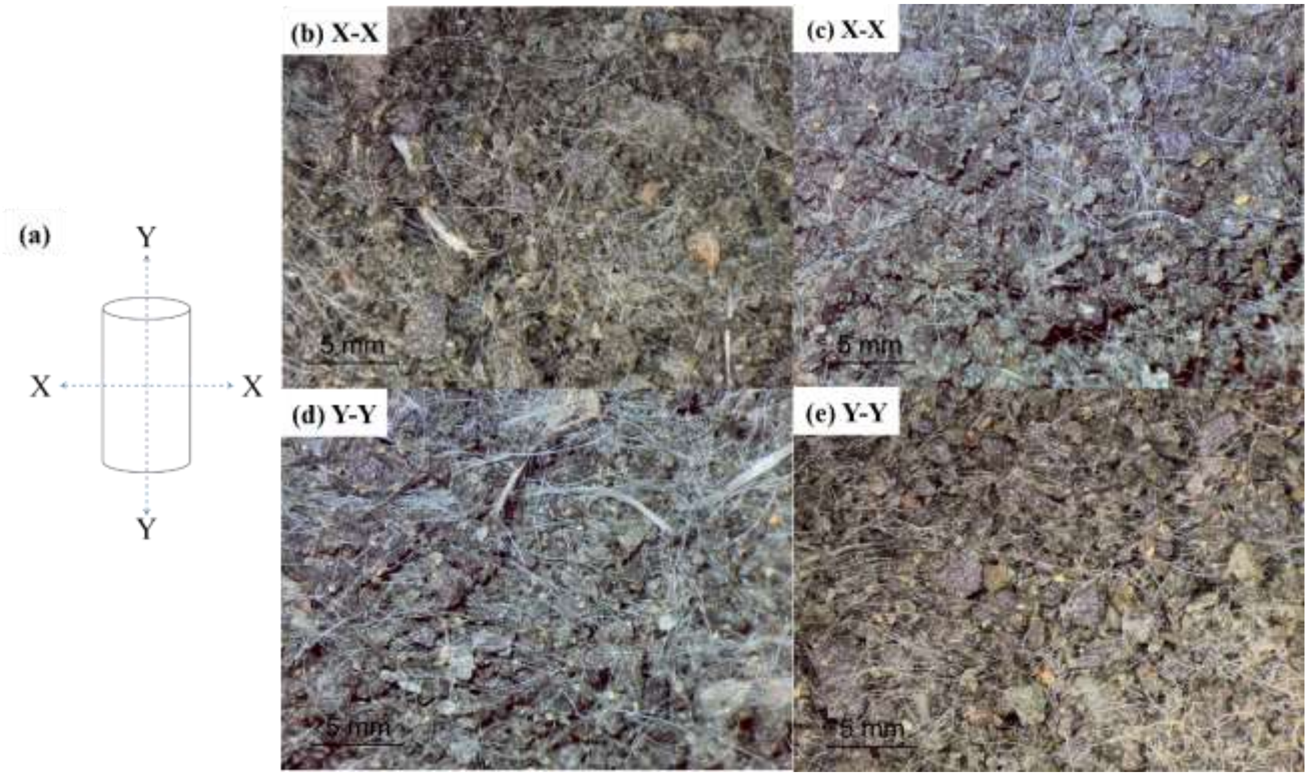

Figure 4. Microscope images of BS1 with 0.5% fibers taken at different cross-sections

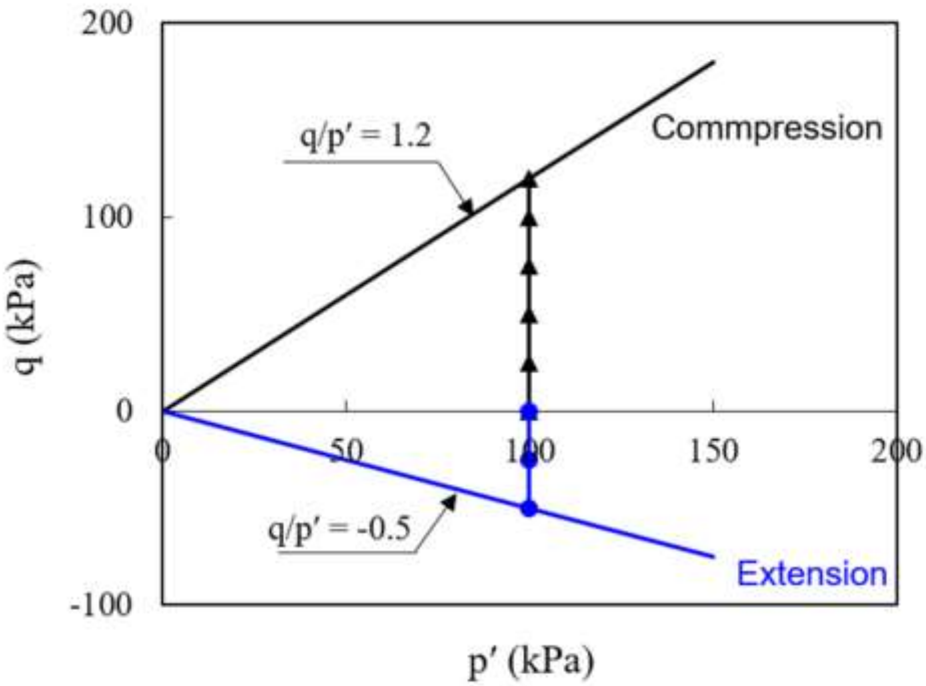

Figure 5. Illustration of stress paths applied in the present study

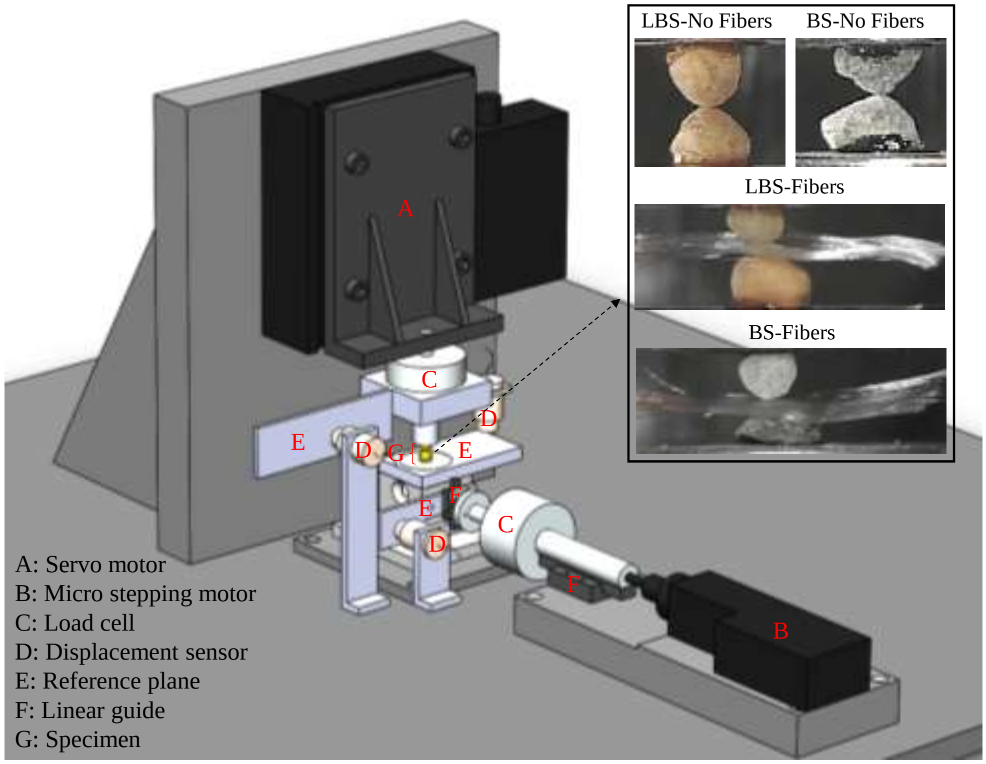

Figure 6. Grain-scale experimental setup used to investigate the sand-fiber-sand interactions at the small scale

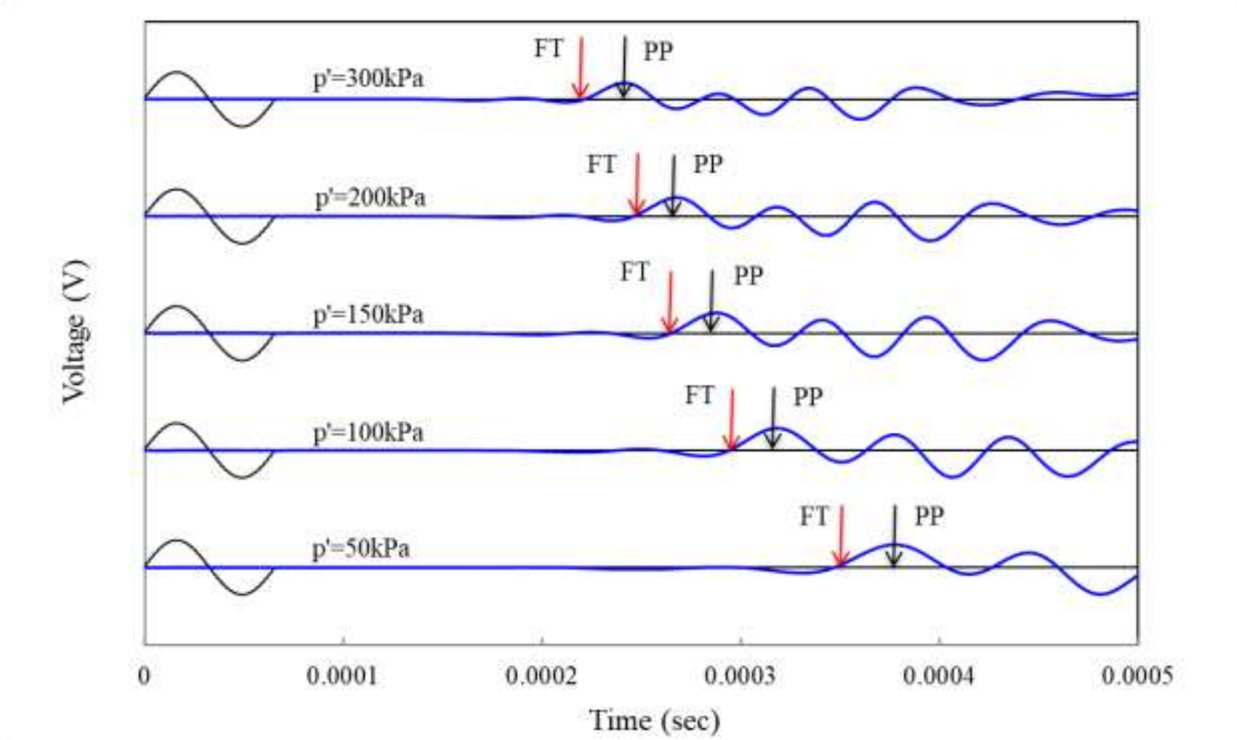

Figure 7. Example of signal analysis during the propagation of waves in the specimens: Measurement of V_{hh} from lateral bender elements for BS1 with f=15 kHz, (input voltage=14V, p' = 50, 100, 150, 200, 300 kPa) using the first-time of arrival (FT) and peak-to-peak time of arrival (PP) methods

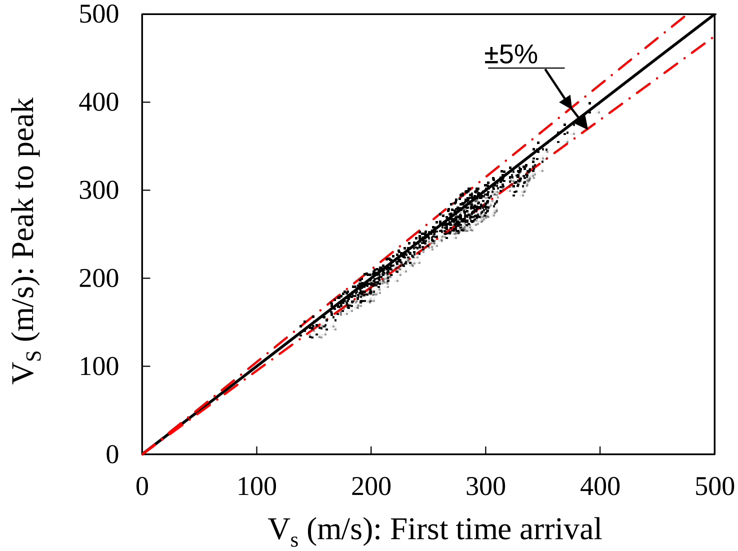

Figure 8. Comparison of the peak-to-peak and first time of arrival methods in the measured shear wave velocities

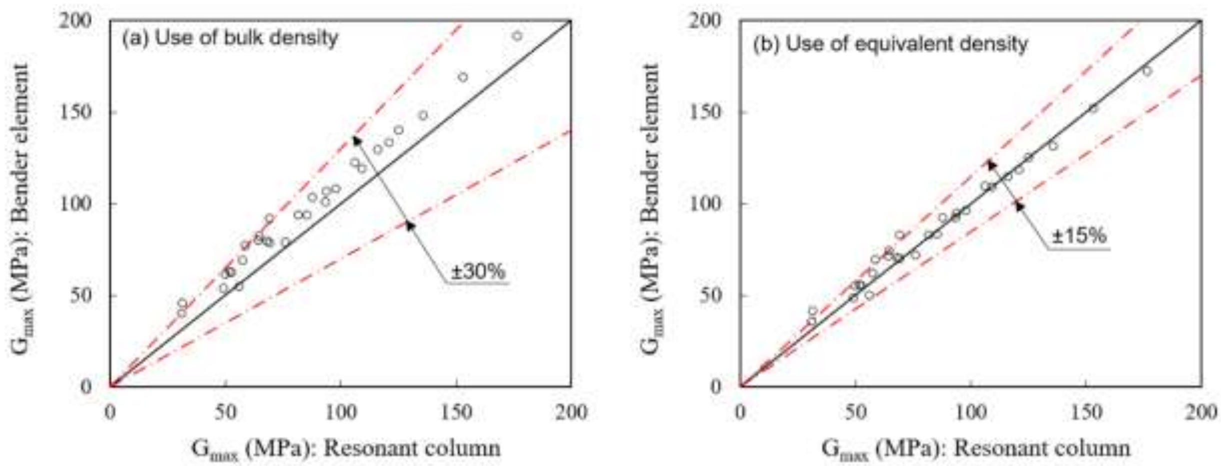

Figure 9. Comparison of estimated elastic stiffness based on resonant column and bender element tests using bulk and equivalent densities

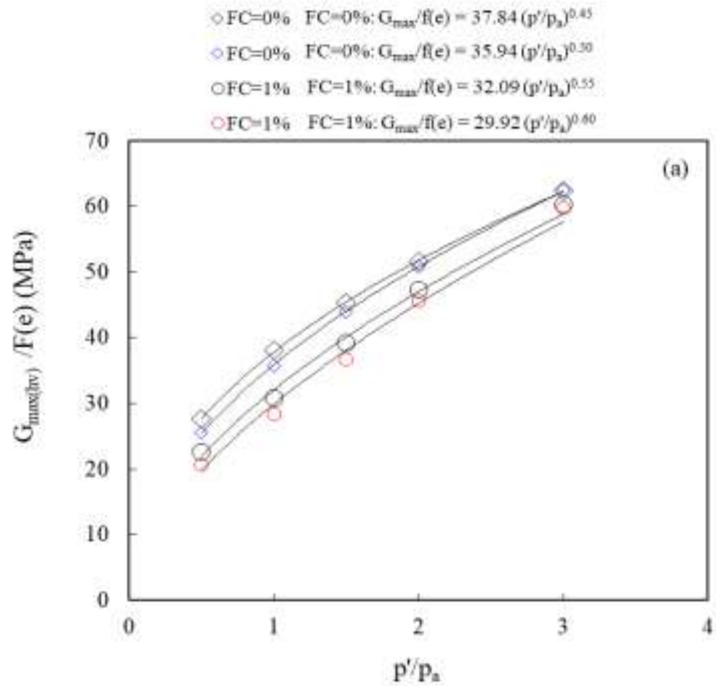

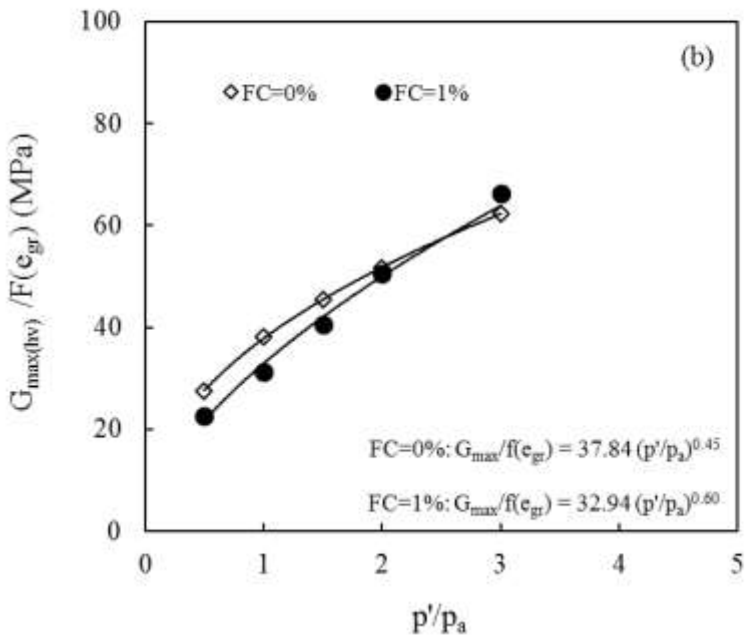

Figure 10. Typical plots of normalized stiffness $G_{max(hv)}$ with respect to (a) a void ratio function and (b) a granular void ratio function against the normalized pressure (data correspond to BS1 as host sand)

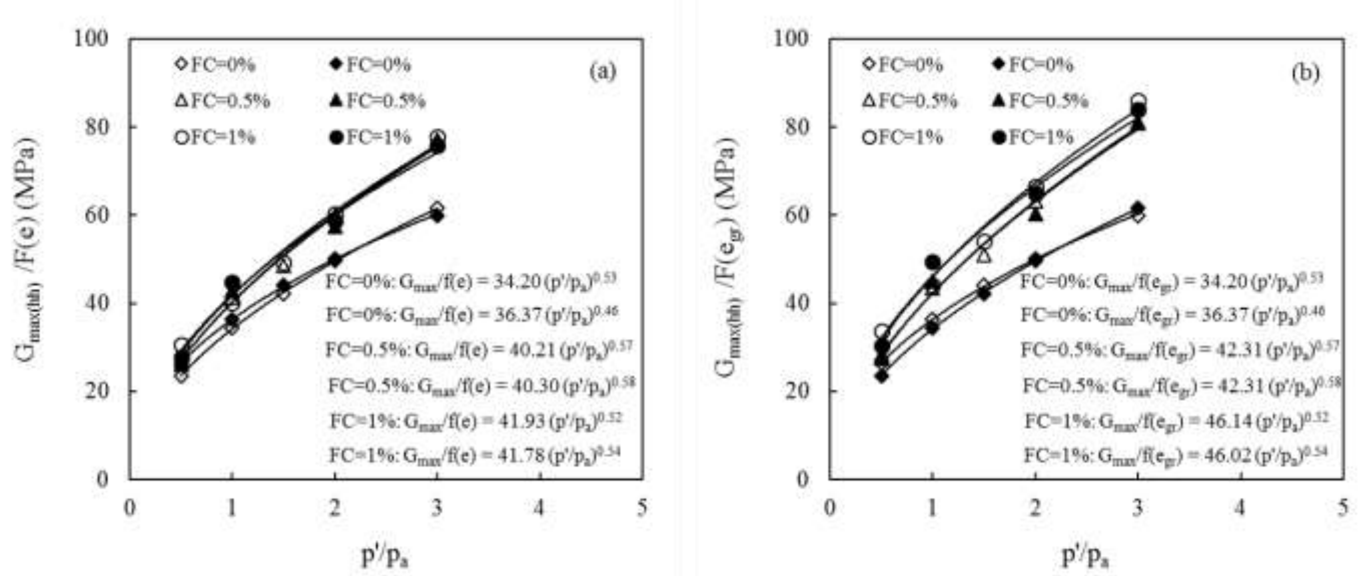

Figure 11. Typical plots of normalized stiffness $G_{max(hh)}$ with respect to (a) a void ratio function and (b) a granular void ratio function against the normalized pressure (data correspond to BS1 as host sand)

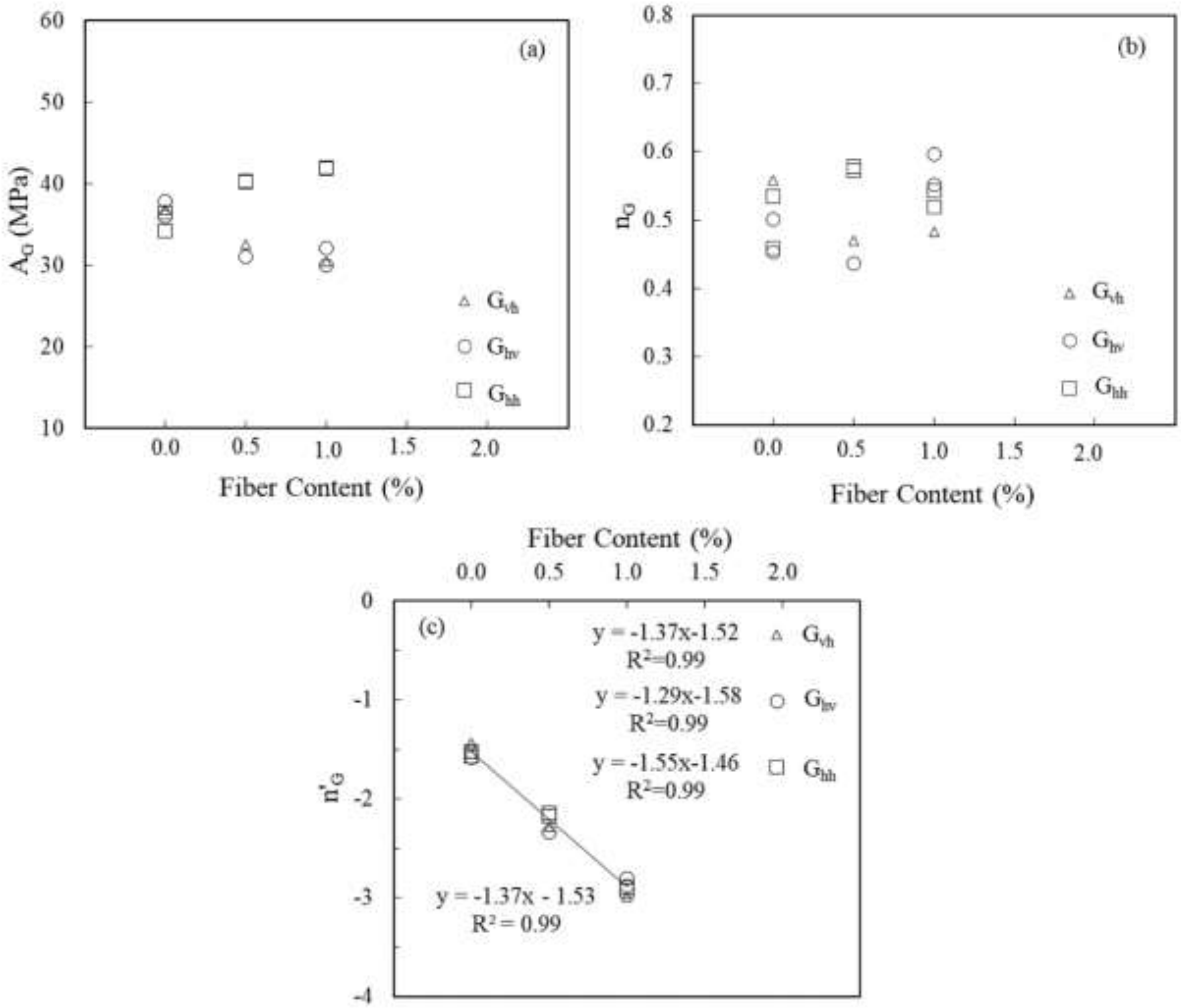

Figure 12. The effect of fiber content on the stiffness model parameters: (a) A_G and (b) n_G (data correspond to BS1 as host sand) (c) Normalized power n'_G against fiber content

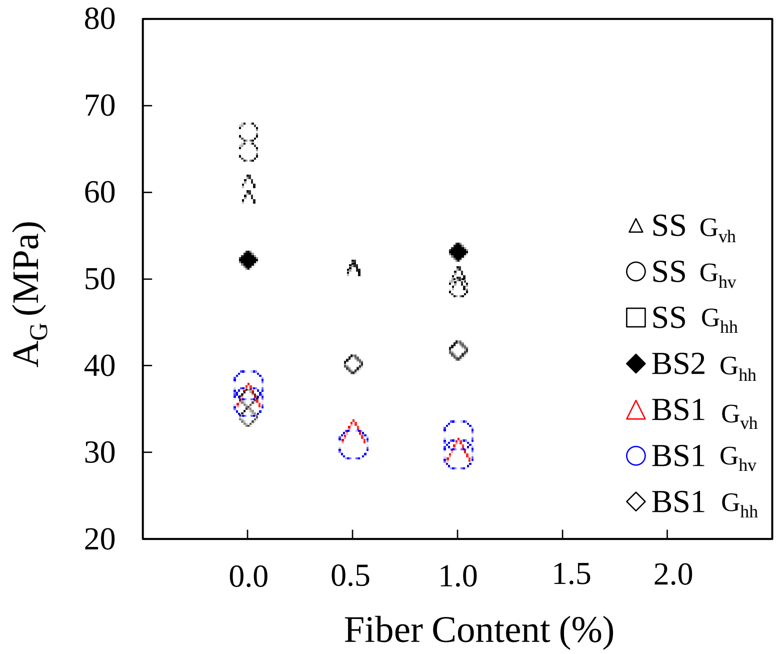

Figure 13. The effect of fiber content on the stiffness model parameter A_G of different sands

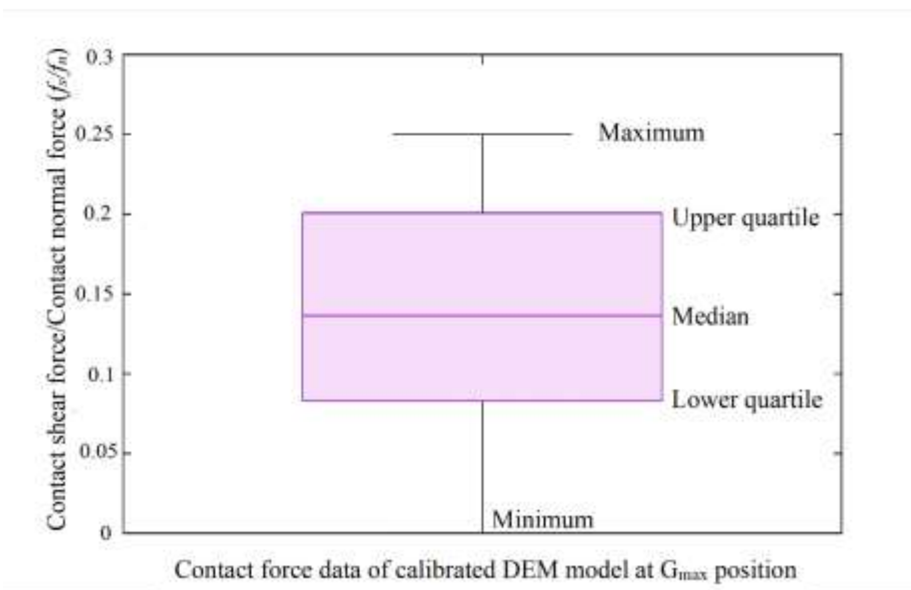

Figure 14. Relative contribution of contact shear and normal forces on a granular assembly (pure sand) depicted at G_{max} from DEM analysis (after Reddy et al. [36])

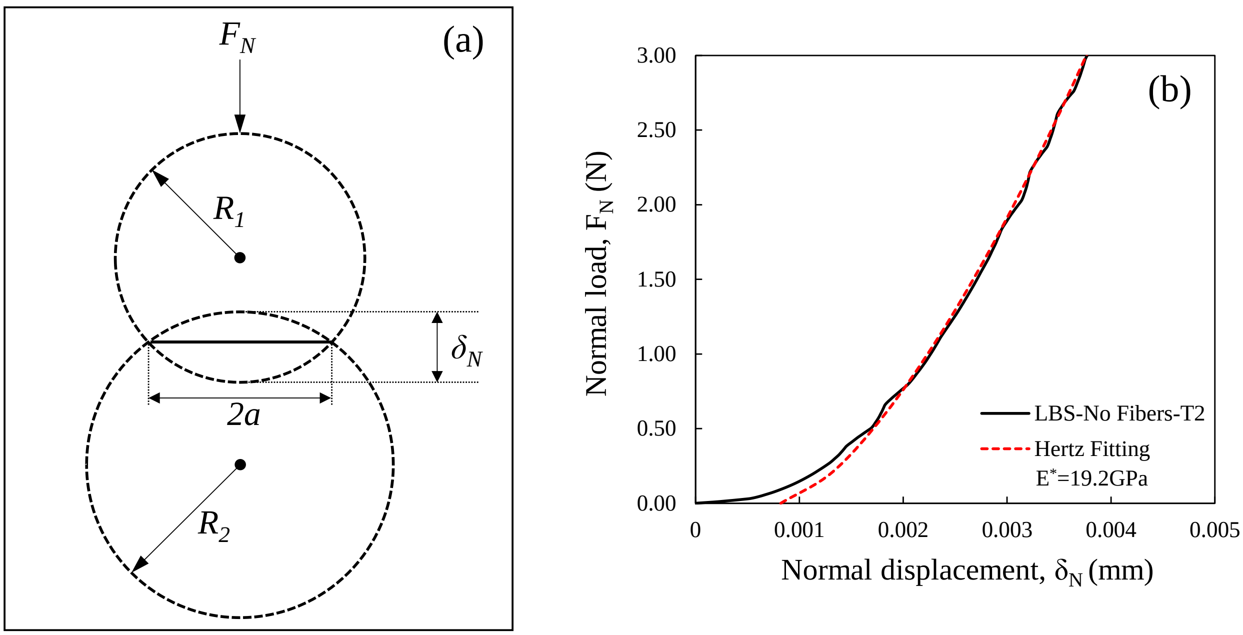

Figure 15. (a) Hertz contact between two spheres (b) representative normal load-displacement experimental curve and theoretical Hertzian fitting curve

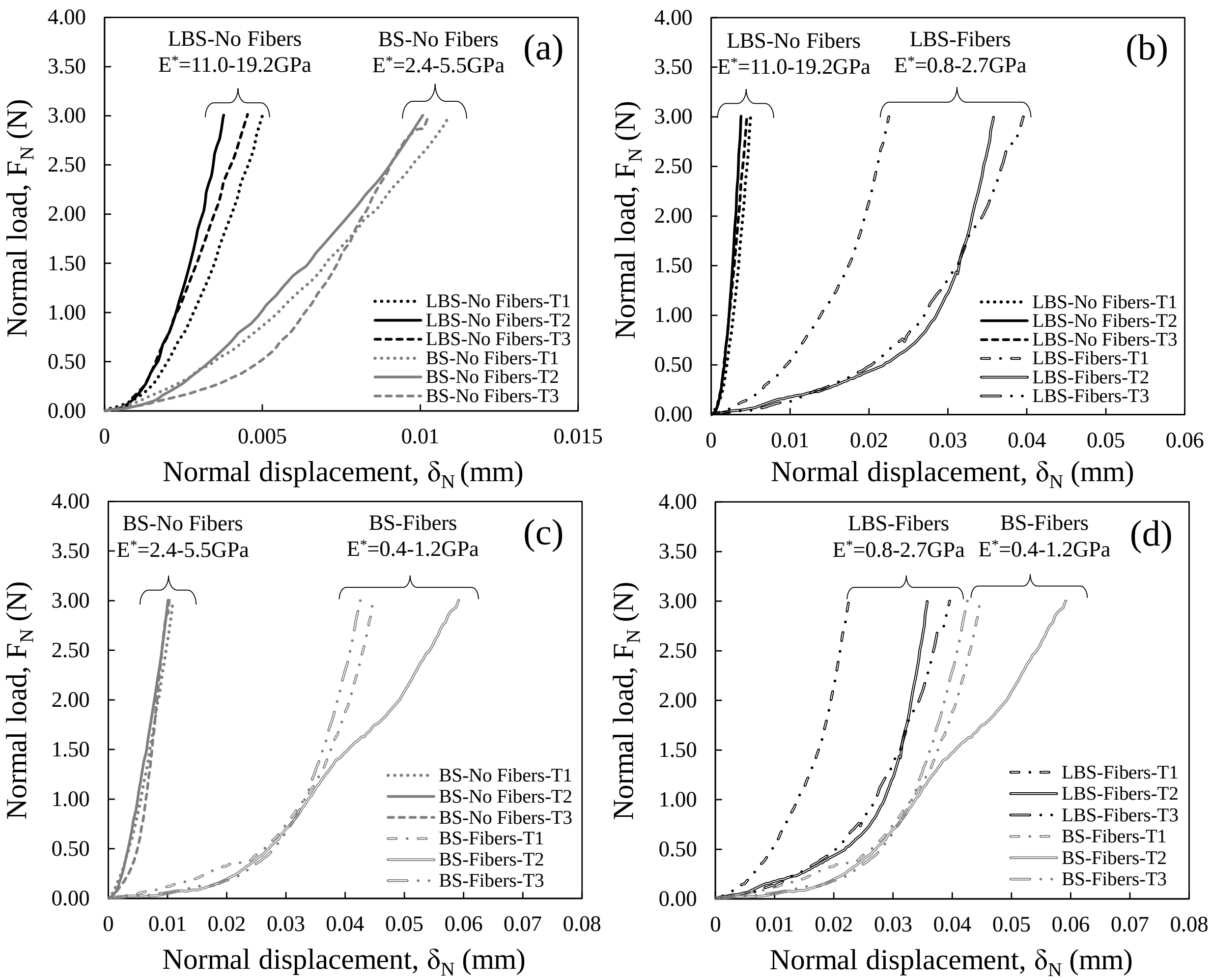

Figure 16. Normal load-displacement behavior among different types of contacts

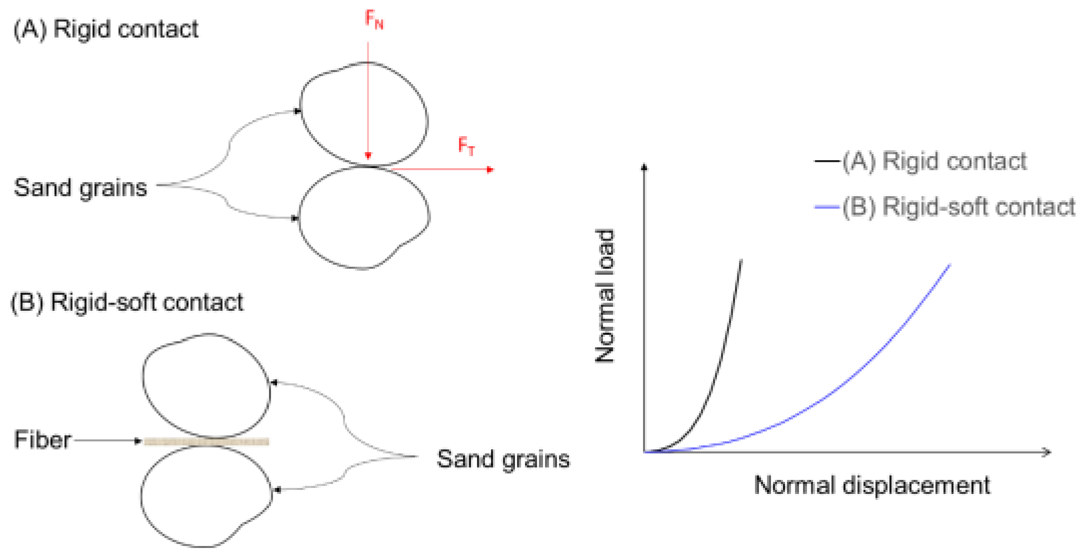

Figure 17. Theoretical illustration on the normal contact response of rigid and rigid-soft interfaces

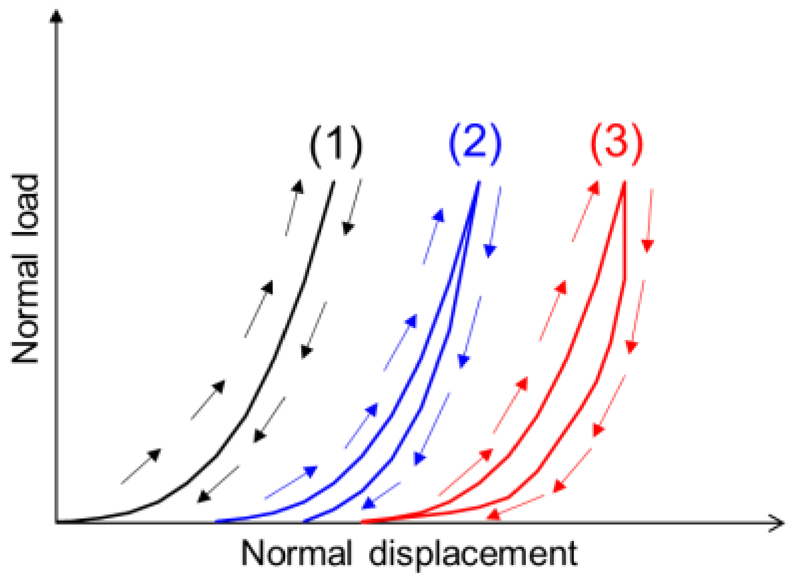

Figure 18. Illustrative examples of fully elastic response. Curve 1: typical example of LBS grains), elastoplastic and hysteretic response. Curve 2: typical example of Blue sand grains), and elastic highly hysteretic behavior. Curve 3: typical example of sand grain-polymeric contacts (after Tian et al. [66] – redrawn by the authors)

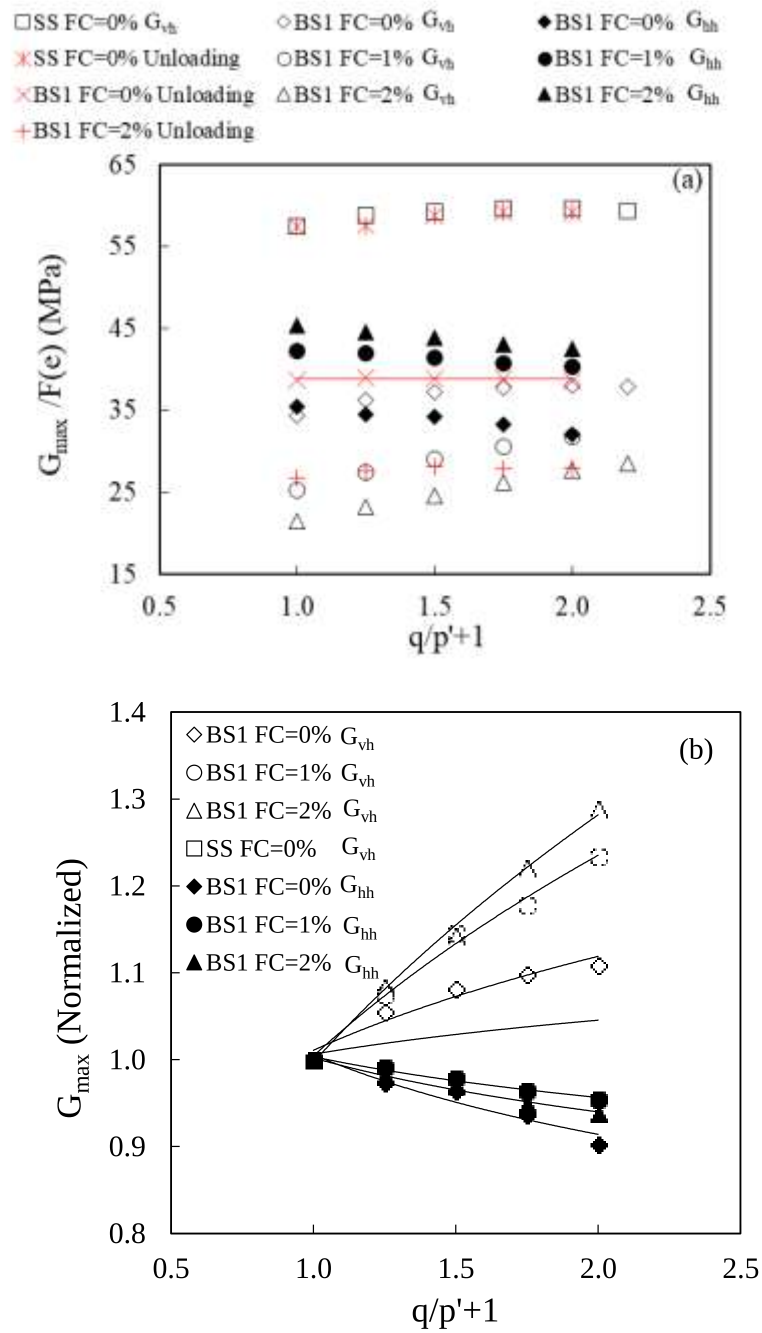

Figure 19. The effect of stress ratio (q/p') and fiber content on (a) normalized stiffness with respect to a void ratio function (b) normalized $G_{max} = [G_{max\,(ani)} / f(e_{ani})] / [G_{max\,(iso)} / f(e_{iso})]$ at p' = 100 kPa

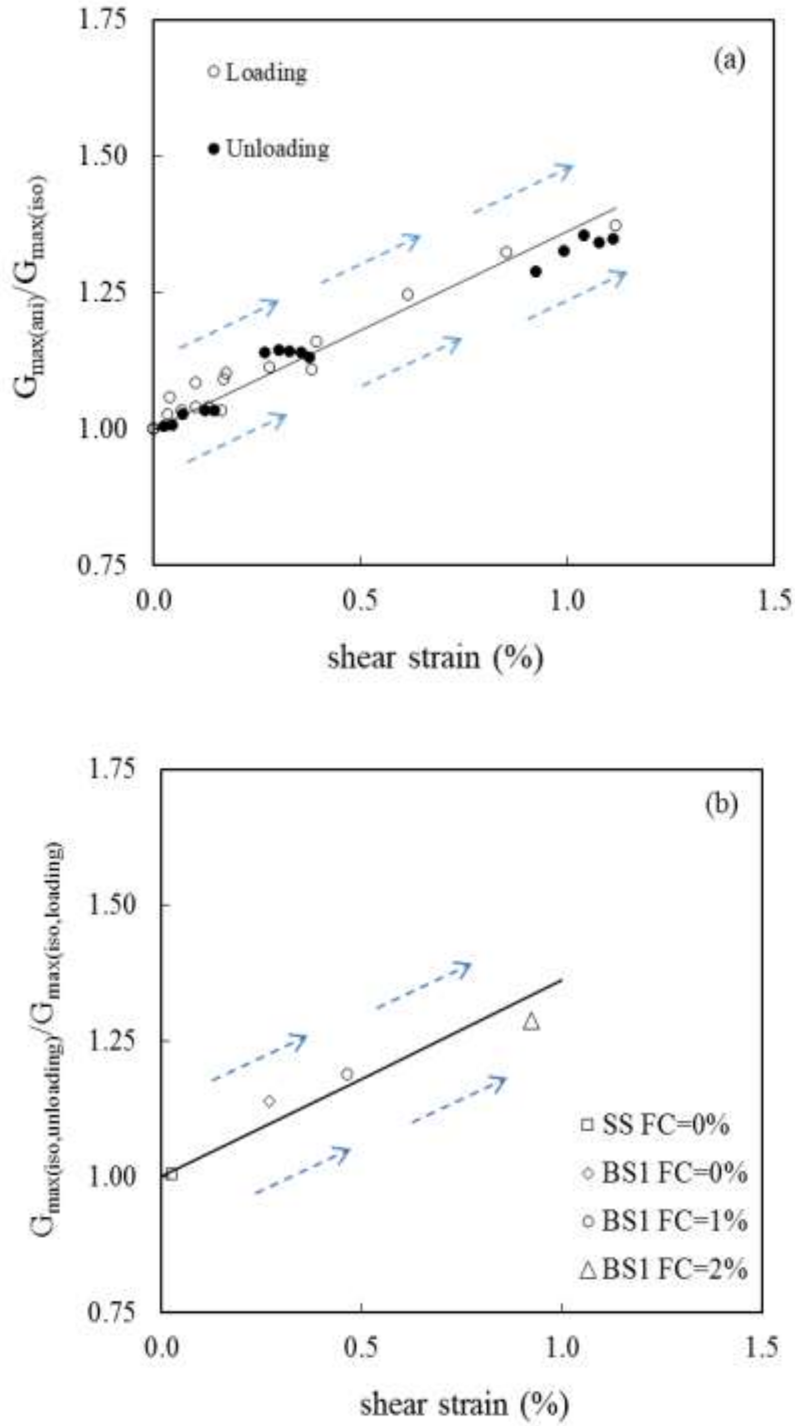

Figure 20. The ratio of (a) $G_{max(ani)}/G_{max(iso,loading)}$ during loading and unloading process (b) $G_{max(iso,unloading)}/G_{max(iso,loading)}$ against shear strain for four different specimens at a constant p'=100 kPa (the values represent $G_{max(vh)}$ in this figure)

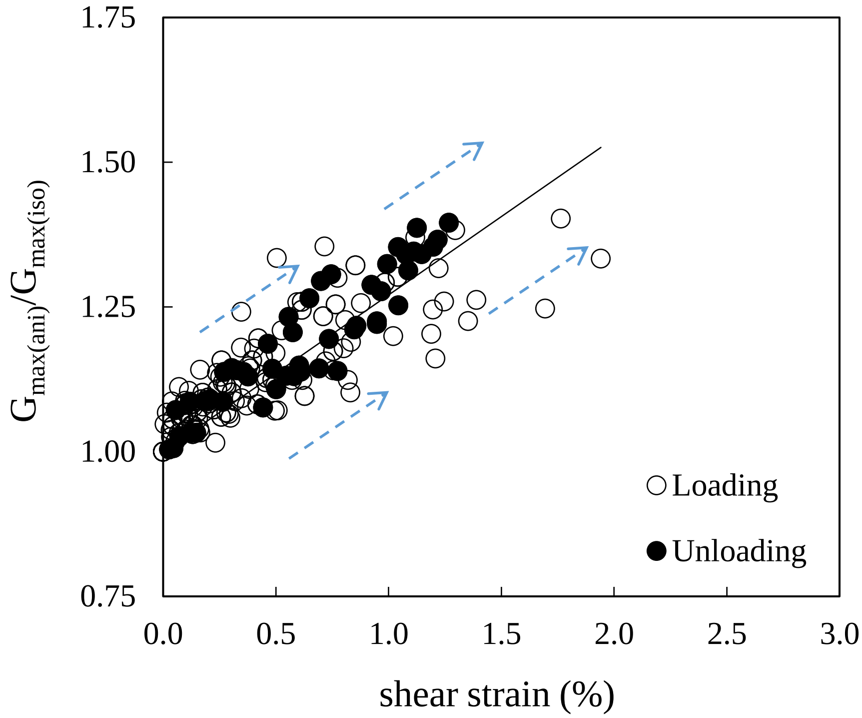

Figure 21. Relationship between the ratio of $G_{max(ani)}/G_{max(iso)}$ and shear strain: The specimens are prepared with different fiber content ranging from 0.5% to 2%, and tested at various effective confining pressures of 50, 100, 400 and 700 kPa (originally the tests were presented by Senetakis and Li [91] and re-analyzed in this study)

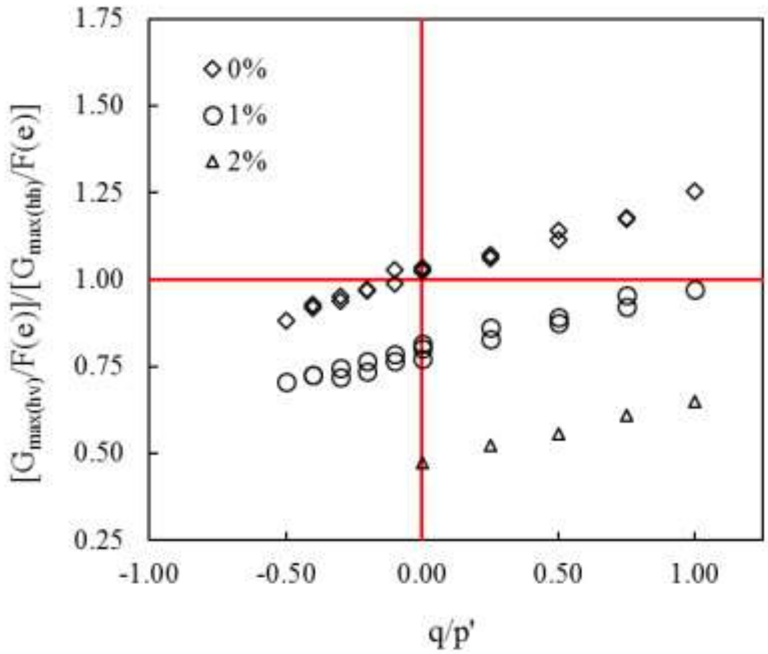

Figure 22. Stiffness ratio of BS1 and BS1 with different fiber contents under extension and compression stress path

Table 1. Basic properties of host sands

Sand Type	Sand Name	Grain Size Distribution			Particle Shape Descriptors*		
		d_{50}(mm)	C_u	C_c	R	S	ρ
Blue Sand 1	BS1	0.99	5.84	1.22	0.28	0.54	0.41
Sydney Sand	SS	0.33	2.18	0.89	0.63	0.68	0.65
Blue Sand 2	BS2	1.03	2.18	0.88	0.28	0.54	0.41

*R: Roundness, S: Sphericity, ρ: Regularity.

Table 2. Testing program and details of specimens subjected to isotropic stress paths

Sample No.	Sand Type	G_{max}	Fiber Content (%)	Sample preparation method	Sample size (mm)	Initial dry density γ_d (kN/m^3)	Initial void ratio e	Initial granular void ratio e_{gr}	Pressure range (kPa)
1	BS1	G_{vh}	0	Dry Compaction	70×140	15.16	0.715	0.715	50-400
2	BS1	G_{hv}	0	Dry Compaction	76×152	16.77	0.550	0.550	50-300
3	BS1	G_{hv}	0	Dry Compaction	76×152	17.26	0.506	0.506	50-300
4	BS1	G_{hh}	0	Dry Compaction	76×152	17.06	0.524	0.524	50-300
5	BS1	G_{hh}	0	Dry Compaction	76×152	17.79	0.461	0.461	50-300
6	BS1	G_{vh}	0.5	Moist Compaction	70×140	15.44	0.667	0.692	50-200
7	BS1	G_{hv}	0.5	Moist Compaction	76×152	15.77	0.633	0.657	50-300
8	BS1	G_{hh}	0.5	Moist Compaction	76×152	16.01	0.608	0.632	50-300
9	BS1	G_{hh}	0.5	Moist Compaction	76×152	15.46	0.666	0.690	50-300
10	BS1	G_{vh}	1	Moist Compaction	70×140	14.99	0.701	0.751	50-200
11	BS1	G_{hv}	1	Moist Compaction	76×152	15.25	0.673	0.722	50-300
12	BS1	G_{hv}	1	Moist Compaction	76×152	15.04	0.696	0.746	50-300
13	BS1	G_{hh}	1	Moist Compaction	76×152	15.21	0.677	0.726	50-300
14	BS1	G_{hh}	1	Moist Compaction	76×152	15.30	0.667	0.716	50-300
15	BS2	G_{hh}	0	Moist Compaction	76×152	14.30	0.818	0.818	50-200
16	BS2	G_{hh}	1	Moist Compaction	76×152	13.91	0.834	0.888	50-200
17	SS	G_{vh}	0	Dry Compaction	50×100	14.97	0.737	0.737	50-400
18	SS	G_{vh}	0	Dry Compaction	70×140	16.53	0.573	0.573	50-1600
19	SS	G_{vh}	0.5	Moist Compaction	50×100	14.45	0.782	0.805	50-400
20	SS	G_{vh}	0.5	Moist Compaction	50×100	14.97	0720	0.746	50-300
21	SS	G_{vh}	1	Moist Compaction	50×100	14.35	0.777	0.830	50-400
22	SS	G_{vh}	1	Moist Compaction	50×100	14.48	0.761	0.813	50-300
23	SS	G_{hv}	0	Dry Compaction	76×152	16.77	0.550	0.550	50-500
24	SS	G_{hv}	0	Moist Compaction	76×152	15.28	0.701	0.701	50-500
25	SS	G_{hv}	1	Moist Compaction	76×152	14.85	0.751	0.802	50-500
26	SS	G_{hh}	0	Moist Compaction	76×152	15.10	0.721	0.721	50-500
27	SS	G_{hh}	1	Moist Compaction	76×152	14.56	0.786	0.838	50-500

Table 3. Testing program and details of specimens subjected to anisotropic stress paths

Sample No.	Sand Type	G_{max}	Fiber Content (%)	Sample preparation method	Sample size (mm)	Initial dry density γ_d (kN/m^3)	Initial void ratio e	Initial granular void ratio e_{gr}	Stress ratio q/p'
28	BS1	G_{vh}	0	Dry Compaction	70×140	16.76	0.551	0.551	0-1.2
29	BS1	G_{hh}	0	Dry Compaction	76×152	17.02	0.528	0.528	0-1
30	BS1	G_{vh}	1	Moist Compaction	70×140	15.31	0.666	0.715	0-1.2
31	BS1	G_{hh}	1	Moist Compaction	76×152	15.64	0.646	0.671	0-1
32	BS1	G_{vh}	2	Moist Compaction	70×140	14.22	0.761	0.865	0-1.2
33	BS1	G_{hh}	2	Moist Compaction	76×152	14.30	0.751	0.854	0-1
34	SS	G_{vh}	0	Dry Compaction	50×100	16.09	0.616	0.616	0-1.2
35	BS1	G_{hv}	0	Moist Compaction	76×152	16.37	0.588	0.588	-0.5-1
36	BS1	G_{hh}	0	Moist Compaction	76×152	16.3	0.594	0.594	-0.5-1
37	BS1	G_{hv}	1	Moist Compaction	76×152	14.93	0.709	0.759	-0.5-1
38	BS1	G_{hh}	1	Moist Compaction	76×152	15.47	0.649	0.697	-0.5-1

Supplementary Table 1. RMS roughness (S_q) measurements on Sydney sand particles based on interferometry analysis

Particle No.	Measurement	S_q (μm)
1	1	0.503
	2	0.385
	3	0.328
	4	0.318
	5	0.399
	6	0.314
	7	0.314
	8	0.664
2	1	0.599
	2	0.433
	3	0.576
	4	0.869
	5	0.431
	6	0.452
	7	0.475
	8	0.728
	9	0.510
Average Value		0.488
Standard Deviation		±0.157

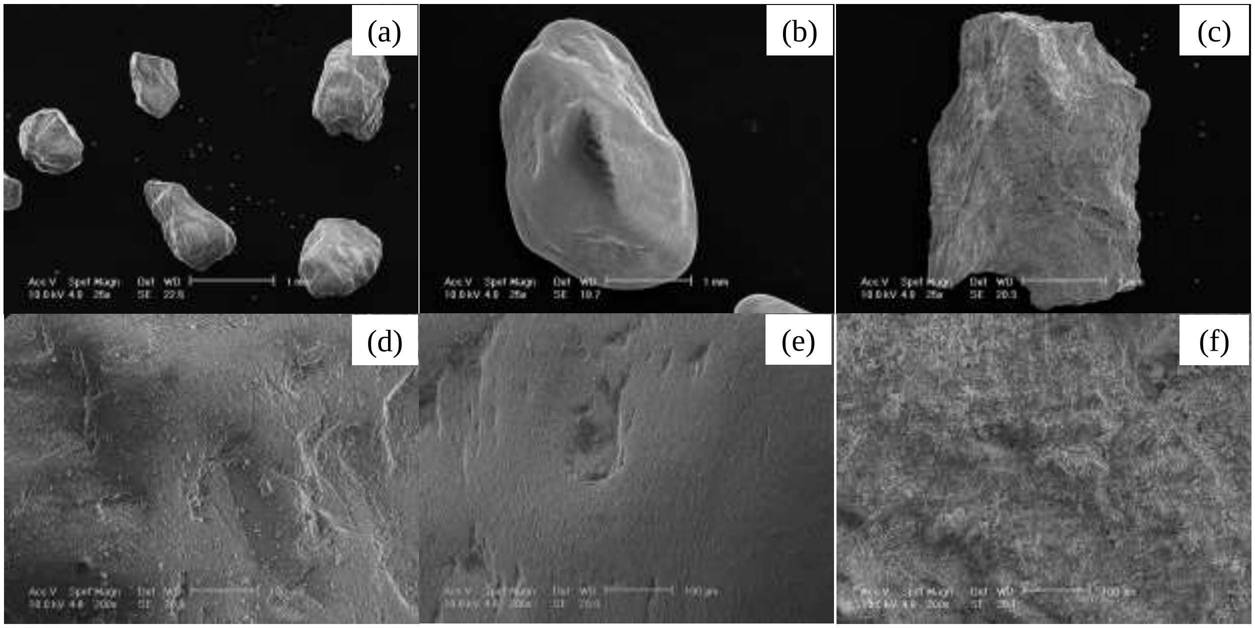

Supplementary Figure 1. SEM photos (a) SS-25x (b) LBS-25x (c) BS-25x (d) SS-200x (e) LBS-200x (f) BS-200x (SS: Sydney sand, LBS: Leighton Buzzard sand, BS: Blue sand)

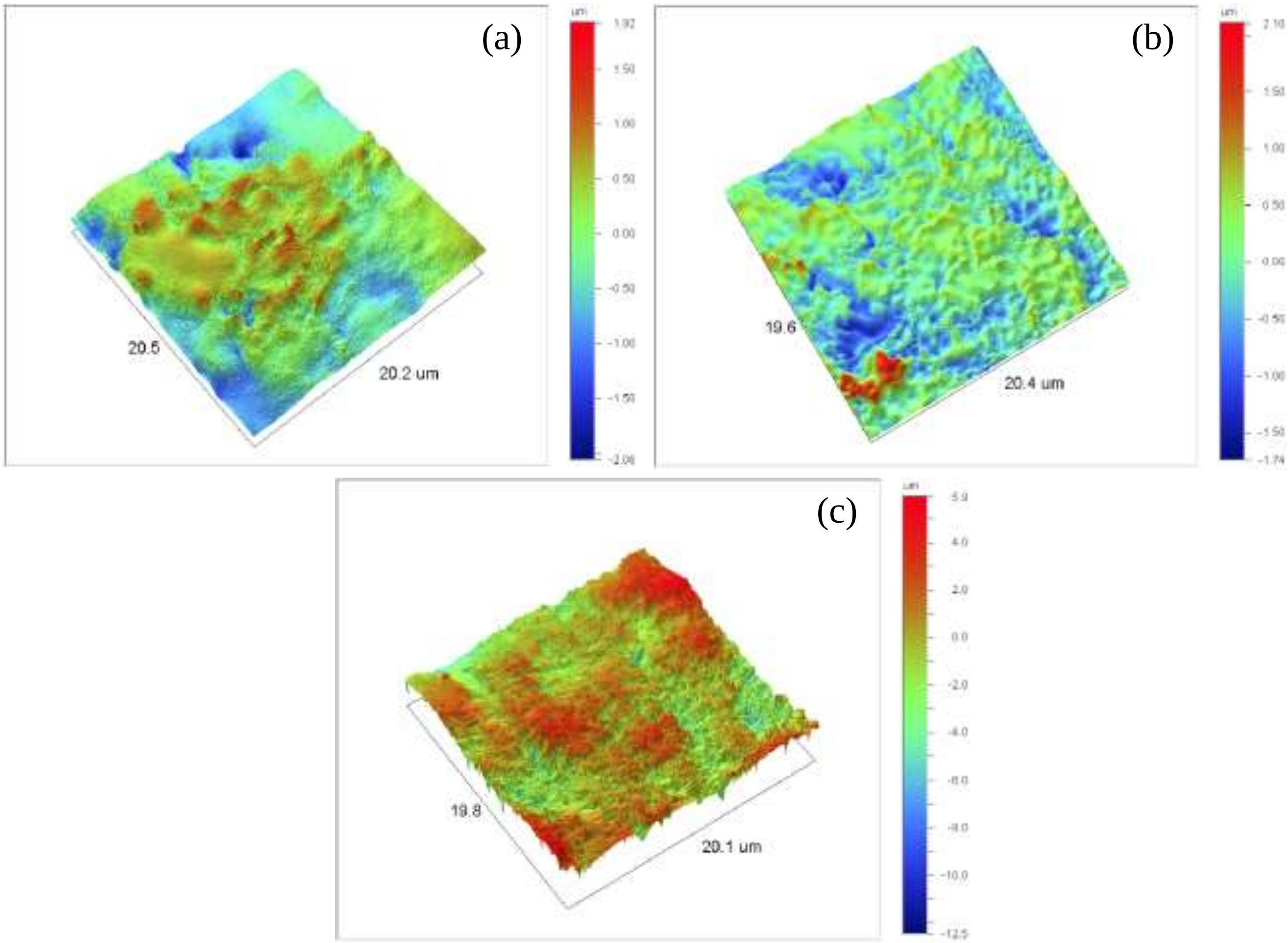

Supplementary Figure 2. Optical surface profiles of representative particles from (a) SS (b) LBS (c) BS

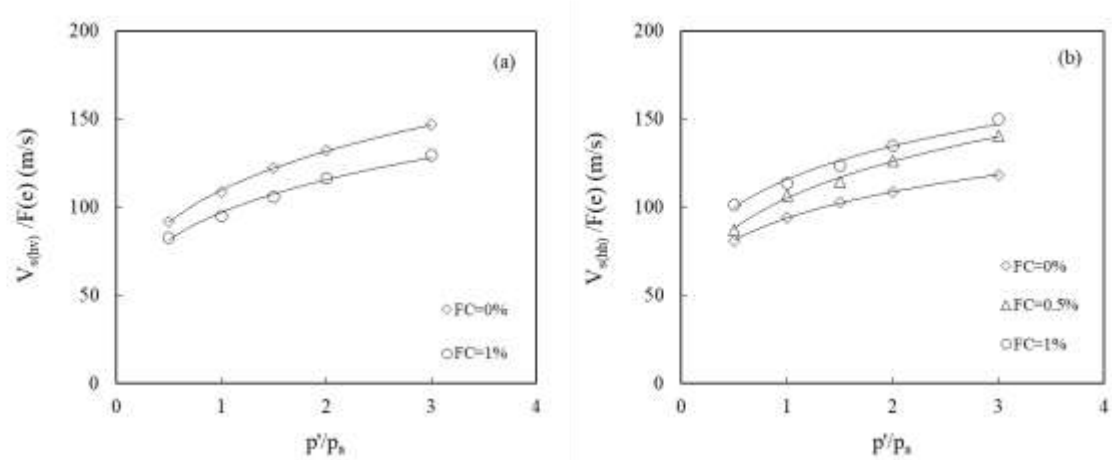

Supplementary Figure 3. Typical plots of normalized shear wave velocity (a)$v_{(hv)}$ (b) $v_{(hh)}$ with respect to a void ratio function against the normalized pressure (data correspond to BS1 as host sand)